Disintegration and Buttressing Effect of the Landfast Sea Ice in the Larsen B Embayment, Antarctic Peninsula

Yudong Sun[1], Bryan Riel[2], and Brent Minchew[2]

[1]Massachusetts Institute of Techno
[2]Massachusetts Institute of Technology

April 16, 2023

Abstract

The speed-up of glaciers following ice shelf collapse can accelerate ice mass loss dramatically. Investigating the deformation of landfast sea ice enables studying its resistive (buttressing) stresses and mechanisms driving ice collapse. Here, we apply offset tracking to Sentinel-1 A/B synthetic aperture radar (SAR) data to obtain a 2014-2022 time-series of horizontal velocity and strain rate fields of landfast ice filling the embayment formerly covered by the Larsen B Ice Shelf, Antarctic Peninsula until 2002. The landfast ice disintegrated in 2022, and we find that it was precipitated by a few large opening rifts. Upstream glaciers did not accelerate after the collapse, which implies little buttressing effect from landfast ice, a conclusion supported by the near-zero correlation between glacier velocity and landfast ice area. Our observations suggest that buttressing stresses are unlikely to be recovered by landfast sea ice over sub-decadal timescales following the collapse of an ice shelf.

Disintegration and Buttressing Effect of the Landfast Sea Ice in the Larsen B Embayment, Antarctic Peninsula

Yudong Sun[1], Bryan Riel[1,2] and Brent Minchew[1]

[1]Department of Earth, Atmospheric, and Planetary Sciences, Massachusetts Institute of Technology, Cambridge, MA, USA
[2]School of Earth Sciences, Zhejiang University, Hangzhou, Zhejiang, China

Key Points:

- We present horizontal velocity and strain rate fields for Larsen B landfast sea ice from 2014 to 2022
- Opening rifts may cause the landfast sea ice to break up
- Landfast sea ice provides negligible buttressing to the upstream glaciers

Corresponding author: Yudong Sun, yudong@mit.edu

Abstract

The speed-up of glaciers following ice shelf collapse can accelerate ice mass loss dramatically. Investigating the deformation of landfast sea ice enables studying its resistive (buttressing) stresses and mechanisms driving ice collapse. Here, we apply offset tracking to Sentinel-1 A/B synthetic aperture radar (SAR) data to obtain a 2014-2022 time-series of horizontal velocity and strain rate fields of landfast ice filling the embayment formerly covered by the Larsen B Ice Shelf, Antarctic Peninsula until 2002. The landfast ice disintegrated in 2022, and we find that it was precipitated by a few large opening rifts. Upstream glaciers did not accelerate after the collapse, which implies little buttressing effect from landfast ice, a conclusion supported by the near-zero correlation between glacier velocity and landfast ice area. Our observations suggest that buttressing stresses are unlikely to be recovered by landfast sea ice over sub-decadal timescales following the collapse of an ice shelf.

Plain Language Summary

The Antarctic Ice Sheet is a potentially major contributor to sea-level rise due to glaciers' dynamic response to changing oceanic and atmospheric conditions. Its floating extensions, ice shelves, play a critical role in stabilizing the ice sheet by resisting the flow of glaciers that feed into them. However, ice shelves can collapse rapidly. In 2002, a Rhode Island-sized section of the Larsen B Ice Shelf disintegrated, causing adjacent glaciers to speed up. In 2011, landfast sea ice replaced the ice shelf in the Larsen B embayment, but it broke up in 2022. We use remote sensing data to investigate why the landfast ice collapsed and whether it resisted glacier flow as the ice shelf did. We show that opening rifts may be responsible for ice disintegration. We find no detectable buttressing effect from the landfast ice because glaciers did not speed up after removing landfast ice, and seasonal change of landfast ice extent did not affect the grounded glacier velocities. It may be because landfast ice is thinner and easier to deform than the ice shelf. Our observations suggest a possible precursor to ice collapse and highlight the limited role that landfast ice plays in slowing down ice mass loss.

1 Introduction

Acceleration of outlet glaciers in Antarctica can increase rates of sea-level rise. Because of their buttressing effect, ice shelves, which are the floating extensions of the ice sheets, play an essential role in regulating rates of mass loss in glaciers, and thus, sea-level rise (Mercer, 1978; Dupont & Alley, 2005; Bindschadler, 2006; DeConto & Pollard, 2016). More surface melt, basal melt, and iceberg calving can cause thinning, shrinking, and weakening of ice shelves due to the warming of the atmosphere and ocean (Shepherd et al., 2004; Pritchard et al., 2012; Depoorter et al., 2013; Lenaerts et al., 2017; Lai et al., 2020). The disintegration of some ice shelves, such as the Larsen A Ice Shelf in 1995 and Larsen B Ice Shelf in 2002 (both on the Antarctic Penninsula), led to the acceleration of some outlet glaciers by up to eight times the pre-collapse velocity (De Angelis & Skvarca, 2003; Rignot et al., 2004; T. A. Scambos et al., 2004).

From 2011 to 2022, the Larsen B embayment was covered with landfast sea ice, the quasi-stationary sea ice fastened to the coastline or islands (Armstrong (1972); Figure 1a). However, the landfast sea ice collapsed within several days in January 2022. Here, we aim to understand its disintegration mechanism and evaluate the buttressing of the landfast sea ice to determine if it could provide stabilizing effects in the case that ice shelves disintegrate.

We begin by studying the mechanisms for the catastrophic collapse of Larsen B landfast sea ice. Understanding the key mechanisms is important for monitoring the ice shelves, reducing sea-ice-related hazards, and understanding the couplings between the ice sheets,

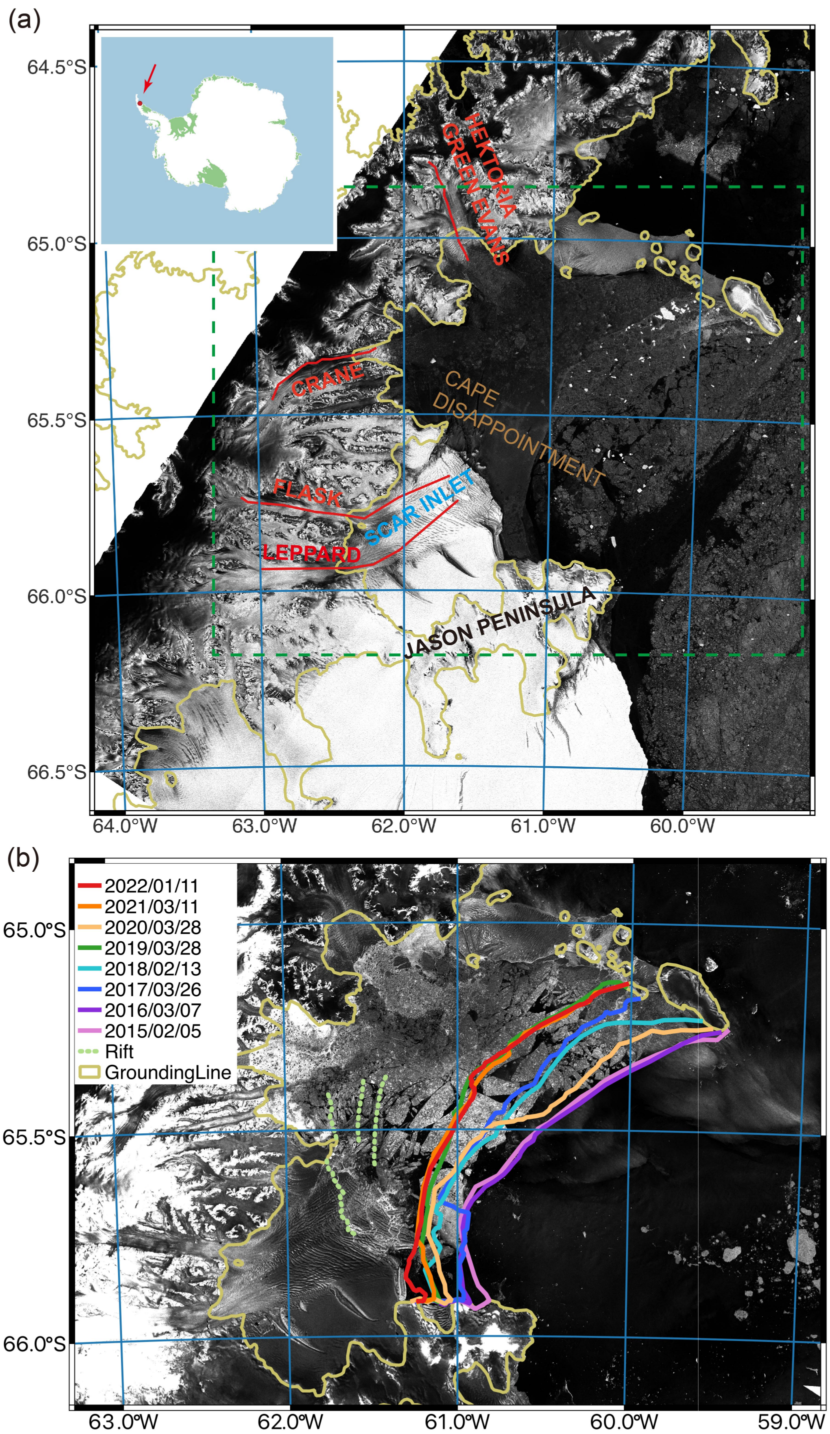

Figure 1. Sentinel-1 SAR amplitude image of the Larsen B area taken on September 30, 2020 (a). SAR image showing collapsed Larsen B landfast ice on January 23, 2022 (b). Yellow lines represent the grounding lines (Rignot et al., 2013; Mouginot et al., 2017). (a) Red lines show the profiles of four glaciers. Red arrow shows the location of our study area in the inserted subfigure. The dark green dash box indicates the approximate region for 1b. (b) Colored lines are the most retreated SLIEs for each year prior to collapse. Light green dashed lines denote the locations of pre-existing rifts.

sea ice, oceans, and the atmosphere. Hydrofracture by surface meltwater (Nye, 1957; Van der Veen, 1998), plate bending by buoyancy forces (Braun & Humbert, 2009; T. Scambos et al., 2009), sea ice loss, ocean swell (Massom et al., 2018), and crevasse-rift system (Glasser & Scambos, 2008; Rack & Rott, 2004) may have caused the disintegration of the Larsen A, B, and Wilkins Ice Shelves. One important observation is the widespread meltwater ponds on the Larsen Ice Shelf before disintegration (van den Broeke, 2005; Sergienko & Macayeal, 2005), possibly related to foehn winds and atmospheric rivers (Cape et al., 2015; Wille et al., 2022). Several models, which consist of densely distributed melt-filled crevasses, have been proposed to explain the cascading collapse of ice shelves into small pieces in a short period (MacAyeal et al., 2003; Banwell et al., 2013; Robel & Banwell, 2019). Meltwater ponding is observed every summer on the Larsen B landfast sea ice from Sentinel-1 SAR, Sentinel-2, and MODIS (Moderate Resolution Imaging Spectroradiometer) images. However, the mechanism for landfast sea ice disintegration may differ from the Larsen B Ice Shelf in 2002 due to different mechanical properties of the sea ice (Timco & Weeks, 2010).

Floating ice, restricted laterally by islands, peninsulas, or grounded icebergs, acts like the neck of an hourglass, slowing down the grounded glaciers flowing to the ocean. This buttressing effect can be quantitatively measured by the stress change at the grounding line after the hypothetical removal of the floating ice (Gudmundsson, 2013). It can also be evaluated by using ice-flow models with data assimilation, from which parameters such as stress and viscosity can be estimated. Fürst et al. (2016) estimated the buttressing potential of ice shelves by modeling the second principal horizontal stress (Doake et al., 1998), while Reese et al. (2018) studied it by calculating ice flux change due to the thinning of a given piece of the ice shelf. In terms of landfast ice, Greene et al. (2018) and Gomez-Fell et al. (2022) suggested that it can also buttress the ice shelves because the velocity of the ice shelves strongly correlates with the thickness or extent of landfast ice. In this paper, we adopt this idea to study the buttressing effect of the landfast sea ice that occupied the Larsen B Embayment from 2011 to 2022.

2 Data and methods

We use repeated acquisitions from Sentinel-1 SAR (Supplementary Movie S1) to obtain the relative displacement of the ice surface using the offset tracking technique in the slant-range and azimuth directions, which are perpendicular and parallel to the flight direction, respectively (Strozzi et al., 2002; Joughin, 2002). Next, we use the predicted tide height in the model CATS2008 to remove vertical tidal motions from range displacements to isolate the horizontal displacements. Finally, we use a median filter to smooth the data in the spatial and temporal domains (see details in Supplementary Text S1 Section 1).

To show a cleaner map of velocity, we use two methods. In the first, we smooth the horizontal velocity maps (Supplementary Movie S2) with a second-order Savitzky–Golay filter (Savitzky & Golay, 1964) with a square window size of about 4 km. In the second method, we fit the velocity time-series in the temporal domain to remove the noise and make Movie S3 (horizontal velocity) using the time-series inversion package "iceutils.tseries" (Riel et al., 2014, 2021), which decomposes the signal into secular, seasonal, and transient terms (see details in Supplementary Text S1 Section 3). Movie S2 has a higher spatial resolution, while Movie S3 is less noisy due to the smoothing inherent in the time-series method. Furthermore, we calculate the strain rate maps (Supplementary Movie S4 and S5) from the horizontal velocity maps (Movie S2). Movies S4 and S5 show horizontal dilation strain rate $\dot{\epsilon}_{dilate}$ (the trace of the horizontal strain rate tensor), maximum shear strain rate $\dot{\epsilon}_{shear}$, strain rate along the flow direction $\dot{\epsilon}_{xx}$, and effective strain rate $\dot{\epsilon}_E$ (the second invariant of 3D strain rate tensor), respectively. These terms are defined in Supplementary Text S1 Section 4. To study the temporal change of landfast ice area, we use the cross-correlation method to find the stationary fast ice that moves less than 100 m within 12 days (see details in Supplementary Text S1 Section 2), and delineate the seaward landfast ice edge (SLIE; colored lines in Figure 1b).

3 Results

3.1 Disintegration of landfast sea ice

A time-series of SAR images (collected from Sentinel-1 Path 38) shows the evolution of ice shelves and sea ice (Movie S1). The Larsen B landfast sea ice collapsed into large pieces by January 23, 2022, later drifting counterclockwise on the ocean. It likely broke up between January 19 and 21, inferred from cloudy Moderate Resolution Imaging Spectroradiometer (MODIS) images from NASA's Terra and Aqua satellites. Melange plumes appeared at the end of most glaciers, where ice fragment size is too small to see with SAR. A piece of the Scar Inlet Ice Shelf, comparable in size to the city of Philadelphia, also broke off in this event. This disintegration is different from the 2002 event when only one giant melange plume was observed (Massom et al., 2018). This difference may be due to the sea ice pieces being too thin (Fraser et al., 2021) and too areally extensive to cause fragments to capsize (MacAyeal et al., 2003). After the disintegration, the Hektoria-Green-Evans Glacier retreated and lost about 200 square kilometers in late March (Movie S1).

The sea ice in Antarctica reached a new record low in 2022, probably due to a warmer ocean and strong winds (Raphael & Handcock, 2022). MODIS observed widespread meltwater ponds on the fast ice before disintegration. We investigate the locations of the SLIE every year when the landfast ice extent is the smallest (Figure 1b), which generally retreats landward over the years except 2020. The landfast ice extent reached one of the lowest points just before the collapse in January 2022. The south end of SLIE retreated to the grounded ice (pinning point) near the Jason Peninsula, which also broke off later. Meanwhile, the Philadelphia-size iceberg calved along the opening rift on the Scar Inlet Ice Shelf (green dashed line in Figure 1b). Most broken sea ice pieces near the Cape Disappointment are long and thin rectangles aligned in a similar direction as the rifts. Therefore, we suggest that the four opening rifts we identified in Section 3.3 may contribute to the collapse of the whole landfast ice.

3.2 Landfast sea ice buttressing

This collapsing event provides an opportunity to study the buttressing effect of the landfast sea ice. Some glaciers accelerated up to eightfold about nine months after the collapse of Larsen B Ice Shelf in 2002 (Rignot et al., 2004; T. A. Scambos et al., 2004; Wuite et al., 2015), but it remains unclear whether the sea ice provides enough buttressing stress to meaningfully slow down glaciers. Acceleration of upstream glaciers after the removal of landfast sea ice would show that landfast sea ice in the Larsen B embayment can generate sufficiently high resistive stresses to slow the flow of glaciers. However, the eight months of observations along profiles on four glaciers, which are similar locations as Rignot et al. (2004) (cf. their Figure 3) after the collapse, show no increase in speed (our Figure 2). The speed increase downstream of Hektoria-Green-Evans Glaciers in April (orange dots in Figure 2a) actually reflects the melange plume's speed after the breakup (see details in Movie S1). Because our post-collapse observation time scale spans only eight months, we also analyze the horizontal velocity time-series before the collapse to study its relation with the landfast sea ice extent and buttressing effect.

Figure 3a and Movie S3 illustrate the evolution of velocity, the average of which is about $2 - 3$ m/day in the Larsen B region and increases toward the seaward front. To extract the meaningful signals from the velocity time-series (dots in Figure 3d), we use the inversion method (Riel et al., 2014, 2021) to fit the curves (solid lines). Figure 3d shows a small seasonal variation of velocity for the grounded glacier (red line; A in

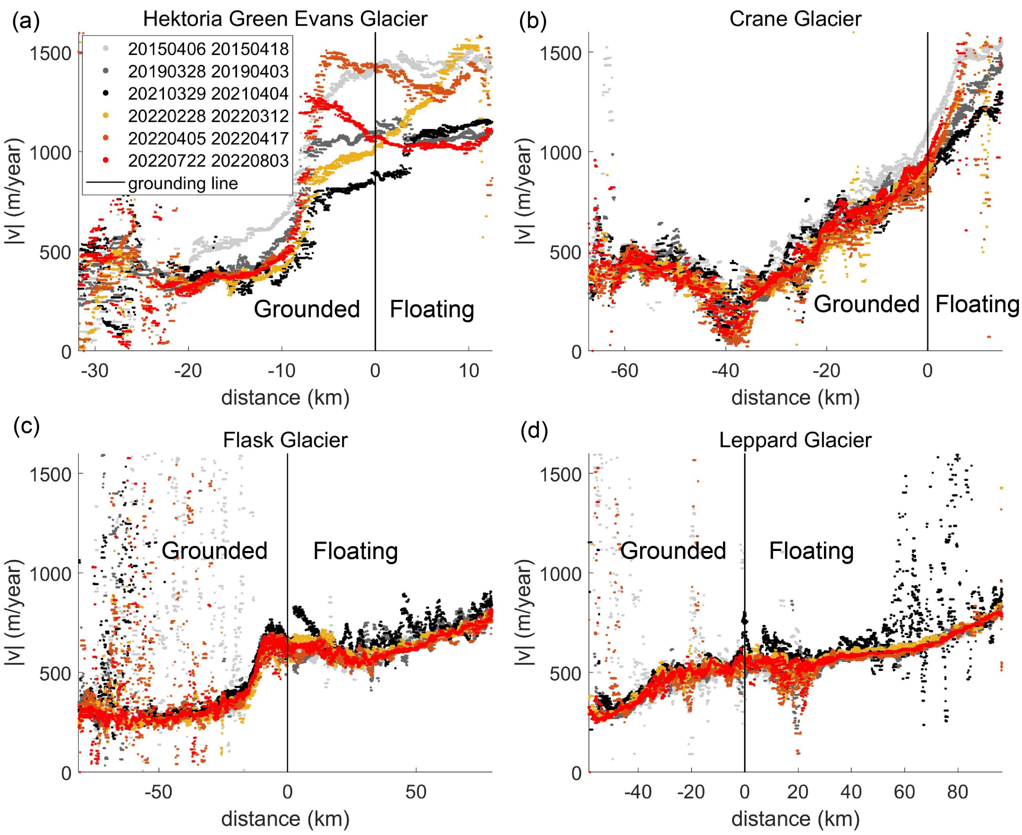

Figure 2. Speed along the profiles (red lines in Figure 1a) for four glaciers. The distance is relative to where the transect crosses the grounding line, with positive values being downstream on the floating ice. Different colors represent pairs for different times (format: yyyymmdd; before collapse: white, gray, and black; after collapse: yellow, orange, and red).

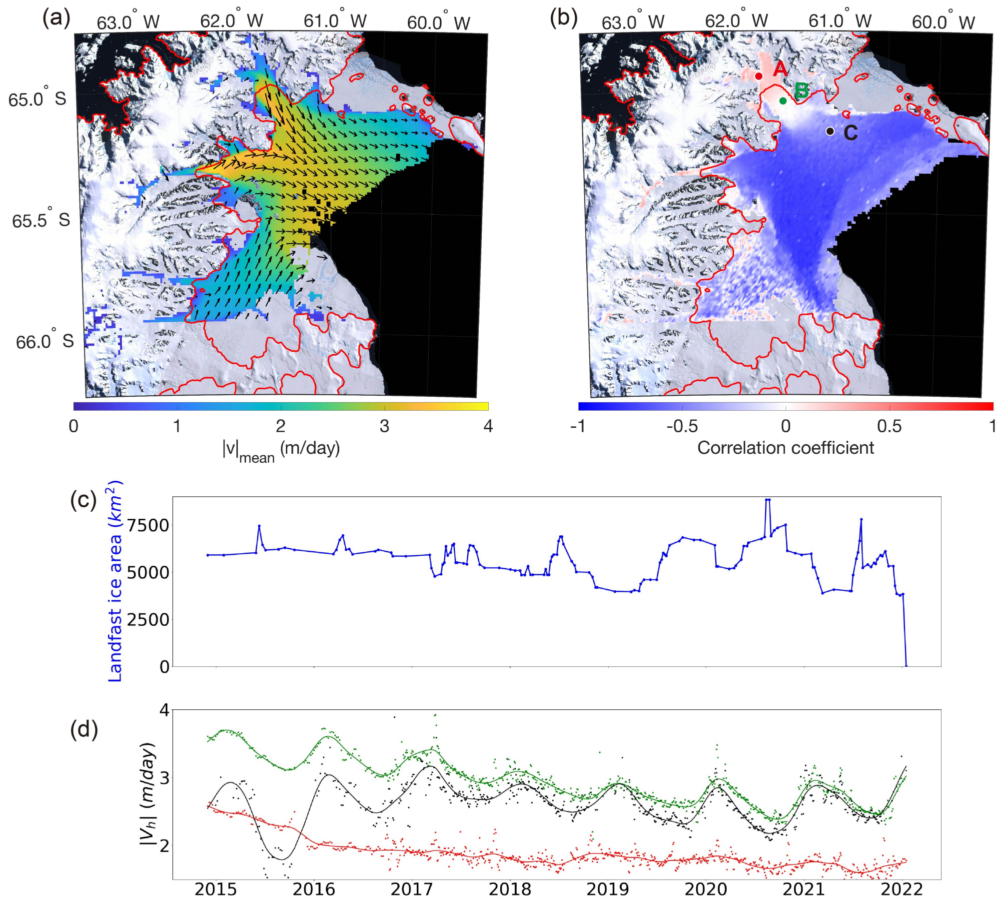

Figure 3. Horizontal velocity after time-series curve fitting and its relation with landfast ice extent. (a) The average horizontal velocity map of Larsen B embayment represented by both the colorbar and vectors. (b) The map of correlation coefficient between speed and landfast sea ice extent. (c) Evolution of the landfast sea ice extent. (d) Time-series of horizontal speed (dots) and fitting lines at 3 locations denoted by dots (Figure 3b). The red lines show the grounding lines and the background map is the Landsat Image Mosaic of Antarctica (Bindschadler et al., 2008) (Figure 3a and b).

Figure 3b). In contrast, the seasonal variation gets larger downstream on the landfast sea ice (green and black lines; B and C in Figure 3b).

To evaluate the buttressing effect, we calculate the correlation coefficient between the landfast sea ice area (Figure 3c) and horizontal velocity. Sea ice adheres to the landfast sea ice, and its area gets larger in winter, while ice breaks away to reduce the areal extent in the summer (Movie S1). The landfast sea ice velocity shown in Figure 3d is higher in summer and lower in winter, so the correlation coefficient is generally negative. Buttressing stress comes from the confined margin of landfast ice with ice shelves, land, or islands (Gudmundsson, 2013; Schoof, 2007). Therefore, it should increase with the contact area between the ice and the solid Earth. We take the areal extent of the sea ice as a proxy for this contact area. Thus, if the velocity variation of the upstream glaciers negatively correlates with the extent of the landfast sea ice, the sea ice has a "tele-buttressing" effect, as discussed in Reese et al. (2018). We use a fitting curve from time-series inversion (Supplementary Text S1 Section 3) to do the correlation because the high-frequency signals (with periods shorter than 10 days) are removed, giving a similar sampling rate to the fast ice extent data.

We show correlation coefficients for every location where velocity data are available more than 50% of the time (Figure 3b). The correlation coefficient is negative on the landfast sea ice, while it is near 0 on the glacier outlets and slightly below 0 on the Scar Inlet Ice Shelf. The slight positive correlation on the Hecktoria-Green-Evans glacier is due to the decreasing trend of velocity (Figure 3d). Our results suggest that the buttressing stress from the Larsen B landfast sea ice may not transmit to the upstream glaciers due to a combination of thinner ice with different mechanical properties and materials damaged from the previous long-lived ice shelves (Domack et al., 2005). This result agrees with the observation of no speed-up after the removal. At this time, it is not clear how to estimate the relative importance of buttressing of ice thickness and differing mechanical properties between the sea ice pack and the Larsen B Ice Shelf, only to say that the sea ice pack provided little buttressing relative to the ice shelf.

3.3 Rift and pressure ridge

The SLIE in Larsen B usually retreats from autumn to winter and advances from spring to summer (blue line in Figure 3c). To study these processes and corresponding rifts and pressure ridges, we take the gradient of the spatially-smoothed velocity field to produce the strain maps (Movie S4 and S5; method discussed in Text S1 Section 4). The strain-rate maps ($\dot{\epsilon}_{dilate}$ in Movie S4) show high compressional strain rates (blue) at the boundary when the drift ice sticks to the landfast ice. This signal indicates the formation of the pressure ridge (Feltham, 2008), which originates from the collision of two pieces of ice driven by wind or ocean currents. We also observe rifts with a high extensional strain rate (red) several days before a piece of ice breaks away from the landfast ice in Movie S4. Therefore, we can consider this phenomenon as a precursor to the ice-calving event.

We show two cases with rifts and pressure ridges inside the landfast sea ice in Figure 4. First, pressure ridges (in blue) showed up at the downstream landfast sea ice of the Hektoria, Crane Glaciers, and Scar Inlet Ice Shelf from June to September in 2015 (Figure 4a). This event happened when the upstream glaciers accelerated (red dots in Figure 3d), so the downstream landfast ice was in compression. If the sea ice is mechanically strong and coherent, there will be a widespread slightly-compressed zone. Therefore, the localized compressional arches indicate that sea ice deforms plastically, and stress becomes independent of strain when it exceeds a certain yield criterion. We suggest this is because sea ice is porous and has low cohesion (Timco & Weeks, 2010; Feltham, 2008; Hibler, 1979).

Second, Figure 4d shows three rifts near Cape Disappointment and one on the Scar Inlet Ice shelf, which emerged during the observation period and probably caused the collapse of the whole landfast sea ice pack (also marked as green dashed lines in Figure 1b). Movie S4 shows that the dilatation strain rate in these rifts is positive continuously, which means they opened plastically after they fractured. The western rift on the landfast sea ice connects with the rift on the ice shelf, which suggests the landfast ice mechanically couples with the ice shelf to some extent. Three opening rifts fractured because the northeast-moving Scar Inlet Ice Shelf protruded into the landfast ice, and it pulled apart the landfast sea ice on the northern side (see velocity directions in Figure 3a). The rift on the front of the Scar Inlet Ice Shelf ruptured because the east-moving landfast ice sheared the indented piece, and the ice shelf was also in an extensional environment. Therefore, these observations suggest that the relative motions of the landfast ice and ice shelf are mainly responsible for the formation of the rifts.

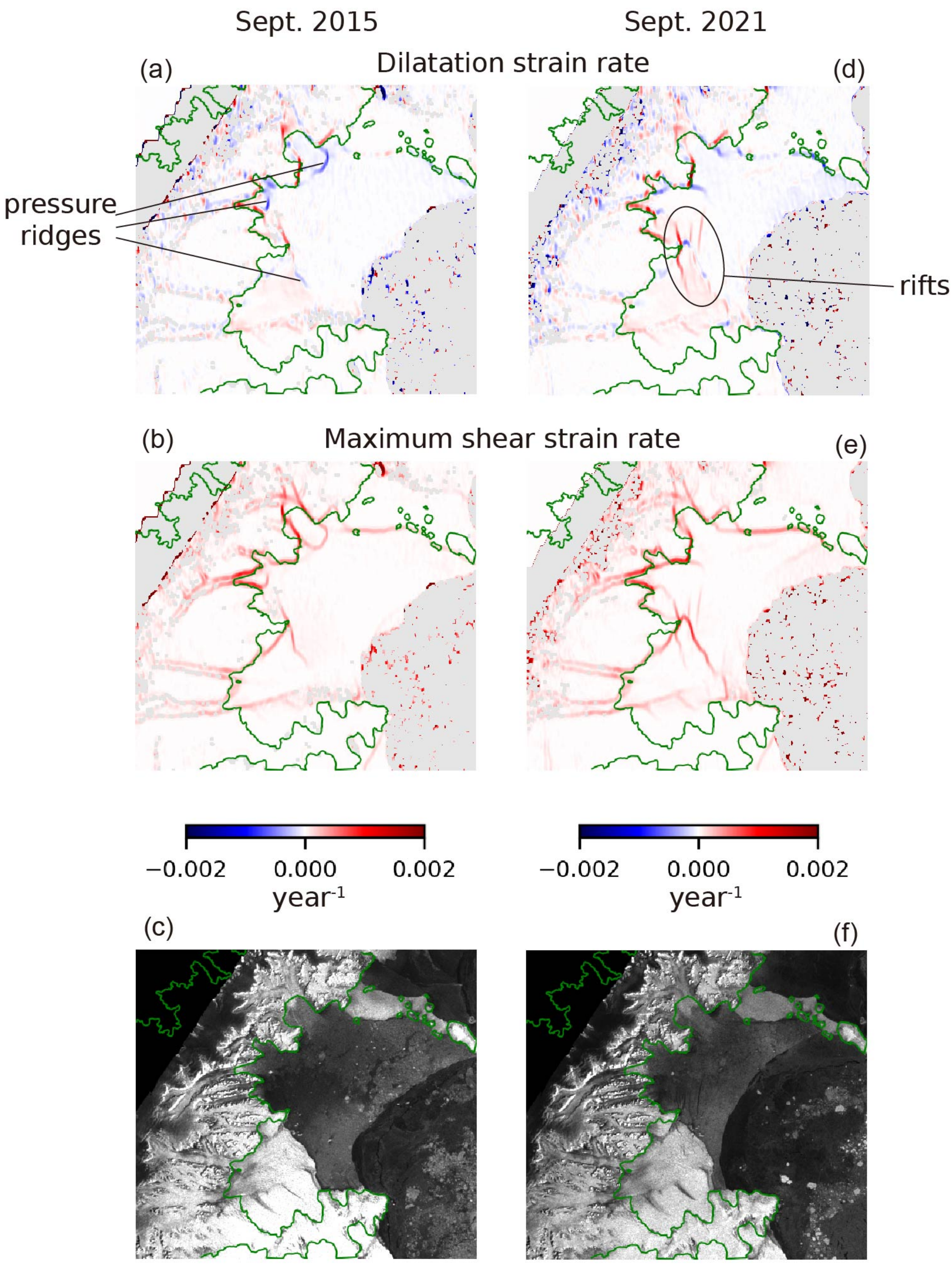

Figure 4. The dialation strain rate $\dot{\epsilon}_{dilate}$, shear strain rate $\dot{\epsilon}_{shear}$ and SAR images in 2015 (a-c) and 2021 (b-f). The strain rate maps represent the deformation between Sept. 9 and Sept. 21, 2015 (a, b), and between Sept. 13 and Sept. 19, 2021 (d, e), respectively. The SAR intensity images are taken on Sept. 21, 2015, and Sept. 19, 2021, respectively. Red represents extension while blue represents compression for the $\dot{\epsilon}_{dilate}$ maps (a, d). Green lines indicate the grounding lines.

4 Discussion and conclusion

The horizontal velocity fields derived from SAR data provide multiple lines of evidence showing that the sea ice pack that filled the Larsen B embayment from 2014 to 2022 provided little buttressing to the grounded glaciers. We find no glacier acceleration after fast ice disintegration and no correlation between glacier velocity and landfast sea ice extent. This is because fast ice is thinner and weaker than the ice shelf that filled the embayment prior to 2002. These characteristics cause landfast sea ice to readily develop large-scale damage features, including the pressure ridges and opening rifts we observe, which reduce the sea ice pack's ability to provide buttressing stresses.

Our argument of negligible buttressing from the sea ice pack is supported by the absence of observable glacier acceleration in the first eight months following the collapse of the ice pack. This result differs from observations following the collapse of the Larsen B Ice Shelf that showed a significant velocity increase on the Crane and Hektoria-Green-Evans Glaciers one year after the collapse (Rignot et al., 2004). We attribute this difference to the fact that the Larsen B Ice Shelf was much thicker and likely more competent at the time of its collapse than the sea ice pack, which allowed the ice shelf to support higher buttressing stresses.

The second piece of evidence is that we find no negative correlation between fast ice extent and velocity on the glaciers. Specifically, the seasonal fluctuation of horizontal velocity is large on the fast ice but is negligibly small on the grounded glaciers and the Scar Inlet Ice Shelf. In contrast, Greene et al. (2018) and Gomez-Fell et al. (2022) found a good correlation between sea ice extent and ice shelf velocity in other areas, probably because their study areas have different geographical locations relative to the ocean and land. For example, the Parker Ice Tongue studied in Gomez-Fell et al. (2022) protrudes into the surrounding sea ice and is thus more sensitive to changes in buttressing at the calving front. Furthermore, the difference between those studies and ours is due to the fact that we also focus on grounded glaciers, which have additional basal drag to resist changes in flow.

We observe the formation of four opening rifts from the strain rate maps (Figure 4d), which may contribute to the disintegration of the whole landfast sea ice. They are much longer than that found on the previous Larsen B Ice Shelf (Glasser & Scambos, 2008), which can undermine the structural integrity of the sea ice pack, further leading to its collapse. We also observe that the fast ice collapsed differently from the ice shelf collapse in 2002. A large melange plume was observed after the collapse in 2002, but the landfast sea ice broke up into large pieces, which implies that sea ice is too thin to capsize and cannot break up in a cascade.

Taken together, the decade-long observations of the Larsen B embayment show that the landfast sea ice that occupied the same area as the Larsen B Ice Shelf did not provide the same buttressing stress as the previous ice shelf, suggesting that if more ice shelves collapse due to climate change, the upstream glaciers will likely accelerate regardless of sea ice conditions. In other words, this finding suggests that ice shelf buttressing is not renewable over sub-decadal timescales. Our observations also elucidate ice-ocean-atmosphere interaction and help to monitor sea-ice-related hazards. For instance, the shrinking landfast sea ice and the large seasonal variation of its horizontal velocity we observe have the potential to illuminate how the ocean and climate influence ice evolution. In addition, the transient signals of high strain rates can be used as precursors for calving events or massive ice collapses.

Open Research Section

We use Copernicus Sentinel-1 synthetic SAR data from 2014 to 2022, retrieved from ASF DAAC and processed by ESA (`https://search.asf.alaska.edu/`). We use the

InSAR Scientific Computing Environment ISCE (Rosen et al., 2012) to perform the pixel offset tracking (https://github.com/isce-framework). The tide model CATS2008 (Padman et al., 2002, 2008) for tide correction is available at https://www.esr.org/research/polar-tide-models/list-of-polar-tide-models/cats2008/. The software "iceutils" (Riel et al., 2014, 2021) for filtering and strain rate calculation is available at https://github.com/bryanvriel/iceutils. We use the software "hyp3_timeseries" (https://github.com/jlinick/hyp3_timeseries) to make Supplementary Movie S1. We use the QGIS (https://qgis.org/en/site/forusers/download.html) and Qantarctica software (https://www.npolar.no/quantarctica/) to plot Figure 1. Our final data products, including velocity and strain rate fields used in Movie S2-S5, are archived in Zenodo (https://doi.org/10.5281/zenodo.7818543).

Acknowledgments

The authors thank Camilla Cattania, Justin Linick, Colin Meyer, Enrico Milanese, Joanna Millstein, Meghana Ranganathan, and Sarah Wells-Moran for helpful discussions. Y.S. received fundings from MIT EAPS Robert R Shrock Fellowship, Sven Treitel (1953) Fellowship, and MIT Mathworks Fellowship. B.M. and B.R. received funding from NSFGEO-NERC grant 1853918, the John W. Jarve (1978) Seed Fund for Science Innovation, and the Earl A Killian III (1978) and Waidy Lee Fund.

References

Armstrong, T. (1972). World meteorological organization. wmo sea-ice nomenclature. terminology, codes and illustrated glossary. edition 1970. geneva, secretariat of the world meteorological organization, 1970.[ix], 147 p.[including 175 photos]+ corrigenda slip.(wmo/omm/bmo, no. 259, tp. 145.). *Journal of Glaciology*, *11*(61), 148–149.

Banwell, A. F., MacAyeal, D. R., & Sergienko, O. V. (2013). Breakup of the larsen b ice shelf triggered by chain reaction drainage of supraglacial lakes. *Geophysical Research Letters*, *40*(22), 5872–5876.

Bindschadler, R. (2006). Hitting the ice sheets where it hurts. *Science*, *311*(5768), 1720–1721.

Bindschadler, R., Vornberger, P., Fleming, A., Fox, A., Mullins, J., Binnie, D., … Gorodetzky, D. (2008). The landsat image mosaic of antarctica. *Remote Sensing of Environment*, *112*(12), 4214–4226.

Braun, M., & Humbert, A. (2009). Recent retreat of wilkins ice shelf reveals new insights in ice shelf breakup mechanisms. *IEEE Geoscience and Remote Sensing Letters*, *6*(2), 263–267.

Cape, M., Vernet, M., Skvarca, P., Marinsek, S., Scambos, T., & Domack, E. (2015). Foehn winds link climate-driven warming to ice shelf evolution in antarctica. *Journal of Geophysical Research: Atmospheres*, *120*(21), 11–037.

De Angelis, H., & Skvarca, P. (2003). Glacier surge after ice shelf collapse. *Science*, *299*(5612), 1560–1562.

DeConto, R. M., & Pollard, D. (2016). Contribution of antarctica to past and future sea-level rise. *Nature*, *531*(7596), 591–597.

Depoorter, M. A., Bamber, J. L., Griggs, J. A., Lenaerts, J. T., Ligtenberg, S. R., van den Broeke, M. R., & Moholdt, G. (2013). Calving fluxes and basal melt rates of antarctic ice shelves. *Nature*, *502*(7469), 89–92.

Doake, C., Corr, H., Rott, H., Skvarca, P., & Young, N. (1998). Breakup and conditions for stability of the northern larsen ice shelf, antarctica. *Nature*, *391*(6669), 778–780.

Domack, E., Duran, D., Leventer, A., Ishman, S., Doane, S., McCallum, S., … Prentice, M. (2005). Stability of the larsen b ice shelf on the antarctic peninsula during the holocene epoch. *Nature*, *436*(7051), 681–685.

Dupont, T., & Alley, R. (2005). Assessment of the importance of ice-shelf buttressing to ice-sheet flow. *Geophysical Research Letters*, *32*(4).

Feltham, D. L. (2008). Sea ice rheology. *Annu. Rev. Fluid Mech.*, *40*, 91–112.

Fraser, A. D., Massom, R. A., Handcock, M. S., Reid, P., Ohshima, K. I., Raphael, M. N., … Porter-Smith, R. (2021). Eighteen-year record of circum-antarctic landfast-sea-ice distribution allows detailed baseline characterisation and reveals trends and variability. *The Cryosphere*, *15*(11), 5061–5077.

Fürst, J. J., Durand, G., Gillet-Chaulet, F., Tavard, L., Rankl, M., Braun, M., & Gagliardini, O. (2016). The safety band of antarctic ice shelves. *Nature Climate Change*, *6*(5), 479–482.

Glasser, N., & Scambos, T. A. (2008). A structural glaciological analysis of the 2002 larsen b ice-shelf collapse. *Journal of Glaciology*, *54*(184), 3–16.

Gomez-Fell, R., Rack, W., Purdie, H., & Marsh, O. (2022). Parker ice tongue collapse, antarctica, triggered by loss of stabilizing land-fast sea ice. *Geophysical Research Letters*, *49*(1), e2021GL096156.

Greene, C. A., Young, D. A., Gwyther, D. E., Galton-Fenzi, B. K., & Blankenship, D. D. (2018). Seasonal dynamics of totten ice shelf controlled by sea ice buttressing. *The Cryosphere*, *12*(9), 2869–2882.

Gudmundsson, G. (2013). Ice-shelf buttressing and the stability of marine ice sheets. *The Cryosphere*, *7*(2), 647–655.

Hibler, W. D. (1979). A dynamic thermodynamic sea ice model. *Journal of physical oceanography*, *9*(4), 815–846.

Joughin, I. (2002). Ice-sheet velocity mapping: a combined interferometric and speckle-tracking approach. *Annals of Glaciology*, *34*, 195–201.

Lai, C.-Y., Kingslake, J., Wearing, M. G., Chen, P.-H. C., Gentine, P., Li, H., … van Wessem, J. M. (2020). Vulnerability of antarctica's ice shelves to meltwater-driven fracture. *Nature*, *584*(7822), 574–578.

Lenaerts, J., Lhermitte, S., Drews, R., Ligtenberg, S., Berger, S., Helm, V., … others (2017). Meltwater produced by wind–albedo interaction stored in an east antarctic ice shelf. *Nature climate change*, *7*(1), 58–62.

MacAyeal, D. R., Scambos, T. A., Hulbe, C. L., & Fahnestock, M. A. (2003). Catastrophic ice-shelf break-up by an ice-shelf-fragment-capsize mechanism. *Journal of Glaciology*, *49*(164), 22–36.

Massom, R. A., Scambos, T. A., Bennetts, L. G., Reid, P., Squire, V. A., & Stammerjohn, S. E. (2018). Antarctic ice shelf disintegration triggered by sea ice loss and ocean swell. *Nature*, *558*(7710), 383–389.

Mercer, J. H. (1978). West antarctic ice sheet and co2 greenhouse effect: a threat of disaster. *Nature*, *271*(5643), 321–325.

Mouginot, J., Scheuchl, B., & Rignot, E. (2017). Measures antarctic boundaries for ipy 2007–2009 from satellite radar, version 2. *National Snow and Ice Data Center*, *10*.

Nye, J. F. (1957). The distribution of stress and velocity in glaciers and ice-sheets. *Proceedings of the Royal Society of London. Series A. Mathematical and Physical Sciences*, *239*(1216), 113–133.

Padman, L., Erofeeva, S. Y., & Fricker, H. A. (2008). Improving antarctic tide models by assimilation of icesat laser altimetry over ice shelves. *Geophysical Research Letters*, *35*(22).

Padman, L., Fricker, H. A., Coleman, R., Howard, S., & Erofeeva, L. (2002). A new tide model for the antarctic ice shelves and seas. *Annals of Glaciology*, *34*, 247–254.

Pritchard, H., Ligtenberg, S. R., Fricker, H. A., Vaughan, D. G., van den Broeke, M. R., & Padman, L. (2012). Antarctic ice-sheet loss driven by basal melting of ice shelves. *Nature*, *484*(7395), 502–505.

Rack, W., & Rott, H. (2004). Pattern of retreat and disintegration of the larsen b ice shelf, antarctic peninsula. *Annals of glaciology*, *39*, 505–510.

Raphael, M. N., & Handcock, M. S. (2022). A new record minimum for antarctic sea ice. *Nature Reviews Earth & Environment*, 1–2.

Reese, R., Gudmundsson, G. H., Levermann, A., & Winkelmann, R. (2018). The far reach of ice-shelf thinning in antarctica. *Nature Climate Change*, *8*(1), 53–57.

Riel, B., Minchew, B., & Joughin, I. (2021). Observing traveling waves in glaciers with remote sensing: new flexible time series methods and application to sermeq kujalleq (jakobshavn isbræ), greenland. *The Cryosphere*, *15*(1), 407–429.

Riel, B., Simons, M., Agram, P., & Zhan, Z. (2014). Detecting transient signals in geodetic time series using sparse estimation techniques. *Journal of Geophysical Research: Solid Earth*, *119*(6), 5140–5160.

Rignot, E., Casassa, G., Gogineni, P., Krabill, W., Rivera, A., & Thomas, R. (2004). Accelerated ice discharge from the antarctic peninsula following the collapse of larsen b ice shelf. *Geophysical research letters*, *31*(18).

Rignot, E., Jacobs, S., Mouginot, J., & Scheuchl, B. (2013). Ice-shelf melting around antarctica. *Science*, *341*(6143), 266–270.

Robel, A. A., & Banwell, A. F. (2019). A speed limit on ice shelf collapse through hydrofracture. *Geophysical Research Letters*, *46*(21), 12092–12100.

Rosen, P. A., Gurrola, E., Sacco, G. F., & Zebker, H. (2012). The insar scientific computing environment. In *Eusar 2012; 9th european conference on synthetic aperture radar* (pp. 730–733).

Savitzky, A., & Golay, M. J. (1964). Smoothing and differentiation of data by simplified least squares procedures. *Analytical chemistry*, *36*(8), 1627–1639.

Scambos, T., Fricker, H. A., Liu, C.-C., Bohlander, J., Fastook, J., Sargent, A., ... Wu, A.-M. (2009). Ice shelf disintegration by plate bending and hydrofracture: Satellite observations and model results of the 2008 wilkins ice shelf break-ups. *Earth and Planetary Science Letters*, *280*(1-4), 51–60.

Scambos, T. A., Bohlander, J., Shuman, C. A., & Skvarca, P. (2004). Glacier acceleration and thinning after ice shelf collapse in the larsen b embayment, antarctica. *Geophysical Research Letters*, *31*(18).

Schoof, C. (2007). Ice sheet grounding line dynamics: Steady states, stability, and hysteresis. *Journal of Geophysical Research: Earth Surface*, *112*(F3).

Sergienko, O., & Macayeal, D. R. (2005). Surface melting on larsen ice shelf, antarctica. *Annals of Glaciology*, *40*, 215–218.

Shepherd, A., Wingham, D., & Rignot, E. (2004). Warm ocean is eroding west antarctic ice sheet. *Geophysical Research Letters*, *31*(23).

Strozzi, T., Luckman, A., Murray, T., Wegmuller, U., & Werner, C. L. (2002). Glacier motion estimation using sar offset-tracking procedures. *IEEE Transactions on Geoscience and Remote Sensing*, *40*(11), 2384–2391.

Timco, G., & Weeks, W. (2010). A review of the engineering properties of sea ice. *Cold regions science and technology*, *60*(2), 107–129.

van den Broeke, M. (2005). Strong surface melting preceded collapse of antarctic peninsula ice shelf. *Geophysical Research Letters*, *32*(12).

Van der Veen, C. (1998). Fracture mechanics approach to penetration of surface crevasses on glaciers. *Cold Regions Science and Technology*, *27*(1), 31–47.

Wille, J. D., Favier, V., Jourdain, N. C., Kittel, C., Turton, J. V., Agosta, C., ... others (2022). Intense atmospheric rivers can weaken ice shelf stability at the antarctic peninsula. *Communications Earth & Environment*, *3*(1), 1–14.

Wuite, J., Rott, H., Hetzenecker, M., Floricioiu, D., De Rydt, J., Gudmundsson, G., ... Kern, M. (2015). Evolution of surface velocities and ice discharge of larsen b outlet glaciers from 1995 to 2013. *The Cryosphere*, *9*(3), 957–969.

Disintegration and Buttressing Effect of the Landfast Sea Ice in the Larsen B Embayment, Antarctic Peninsula

Yudong Sun[1], Bryan Riel[1,2] and Brent Minchew[1]

[1]Department of Earth, Atmospheric, and Planetary Sciences, Massachusetts Institute of Technology, Cambridge, MA, USA
[2]School of Earth Sciences, Zhejiang University, Hangzhou, Zhejiang, China

Key Points:

- We present horizontal velocity and strain rate fields for Larsen B landfast sea ice from 2014 to 2022
- Opening rifts may cause the landfast sea ice to break up
- Landfast sea ice provides negligible buttressing to the upstream glaciers

Corresponding author: Yudong Sun, `yudong@mit.edu`

Abstract

The speed-up of glaciers following ice shelf collapse can accelerate ice mass loss dramatically. Investigating the deformation of landfast sea ice enables studying its resistive (buttressing) stresses and mechanisms driving ice collapse. Here, we apply offset tracking to Sentinel-1 A/B synthetic aperture radar (SAR) data to obtain a 2014-2022 time-series of horizontal velocity and strain rate fields of landfast ice filling the embayment formerly covered by the Larsen B Ice Shelf, Antarctic Peninsula until 2002. The landfast ice disintegrated in 2022, and we find that it was precipitated by a few large opening rifts. Upstream glaciers did not accelerate after the collapse, which implies little buttressing effect from landfast ice, a conclusion supported by the near-zero correlation between glacier velocity and landfast ice area. Our observations suggest that buttressing stresses are unlikely to be recovered by landfast sea ice over sub-decadal timescales following the collapse of an ice shelf.

Plain Language Summary

The Antarctic Ice Sheet is a potentially major contributor to sea-level rise due to glaciers' dynamic response to changing oceanic and atmospheric conditions. Its floating extensions, ice shelves, play a critical role in stabilizing the ice sheet by resisting the flow of glaciers that feed into them. However, ice shelves can collapse rapidly. In 2002, a Rhode Island-sized section of the Larsen B Ice Shelf disintegrated, causing adjacent glaciers to speed up. In 2011, landfast sea ice replaced the ice shelf in the Larsen B embayment, but it broke up in 2022. We use remote sensing data to investigate why the landfast ice collapsed and whether it resisted glacier flow as the ice shelf did. We show that opening rifts may be responsible for ice disintegration. We find no detectable buttressing effect from the landfast ice because glaciers did not speed up after removing landfast ice, and seasonal change of landfast ice extent did not affect the grounded glacier velocities. It may be because landfast ice is thinner and easier to deform than the ice shelf. Our observations suggest a possible precursor to ice collapse and highlight the limited role that landfast ice plays in slowing down ice mass loss.

1 Introduction

Acceleration of outlet glaciers in Antarctica can increase rates of sea-level rise. Because of their buttressing effect, ice shelves, which are the floating extensions of the ice sheets, play an essential role in regulating rates of mass loss in glaciers, and thus, sea-level rise (Mercer, 1978; Dupont & Alley, 2005; Bindschadler, 2006; DeConto & Pollard, 2016). More surface melt, basal melt, and iceberg calving can cause thinning, shrinking, and weakening of ice shelves due to the warming of the atmosphere and ocean (Shepherd et al., 2004; Pritchard et al., 2012; Depoorter et al., 2013; Lenaerts et al., 2017; Lai et al., 2020). The disintegration of some ice shelves, such as the Larsen A Ice Shelf in 1995 and Larsen B Ice Shelf in 2002 (both on the Antarctic Penninsula), led to the acceleration of some outlet glaciers by up to eight times the pre-collapse velocity (De Angelis & Skvarca, 2003; Rignot et al., 2004; T. A. Scambos et al., 2004).

From 2011 to 2022, the Larsen B embayment was covered with landfast sea ice, the quasi-stationary sea ice fastened to the coastline or islands (Armstrong (1972); Figure 1a). However, the landfast sea ice collapsed within several days in January 2022. Here, we aim to understand its disintegration mechanism and evaluate the buttressing of the landfast sea ice to determine if it could provide stabilizing effects in the case that ice shelves disintegrate.

We begin by studying the mechanisms for the catastrophic collapse of Larsen B landfast sea ice. Understanding the key mechanisms is important for monitoring the ice shelves, reducing sea-ice-related hazards, and understanding the couplings between the ice sheets,

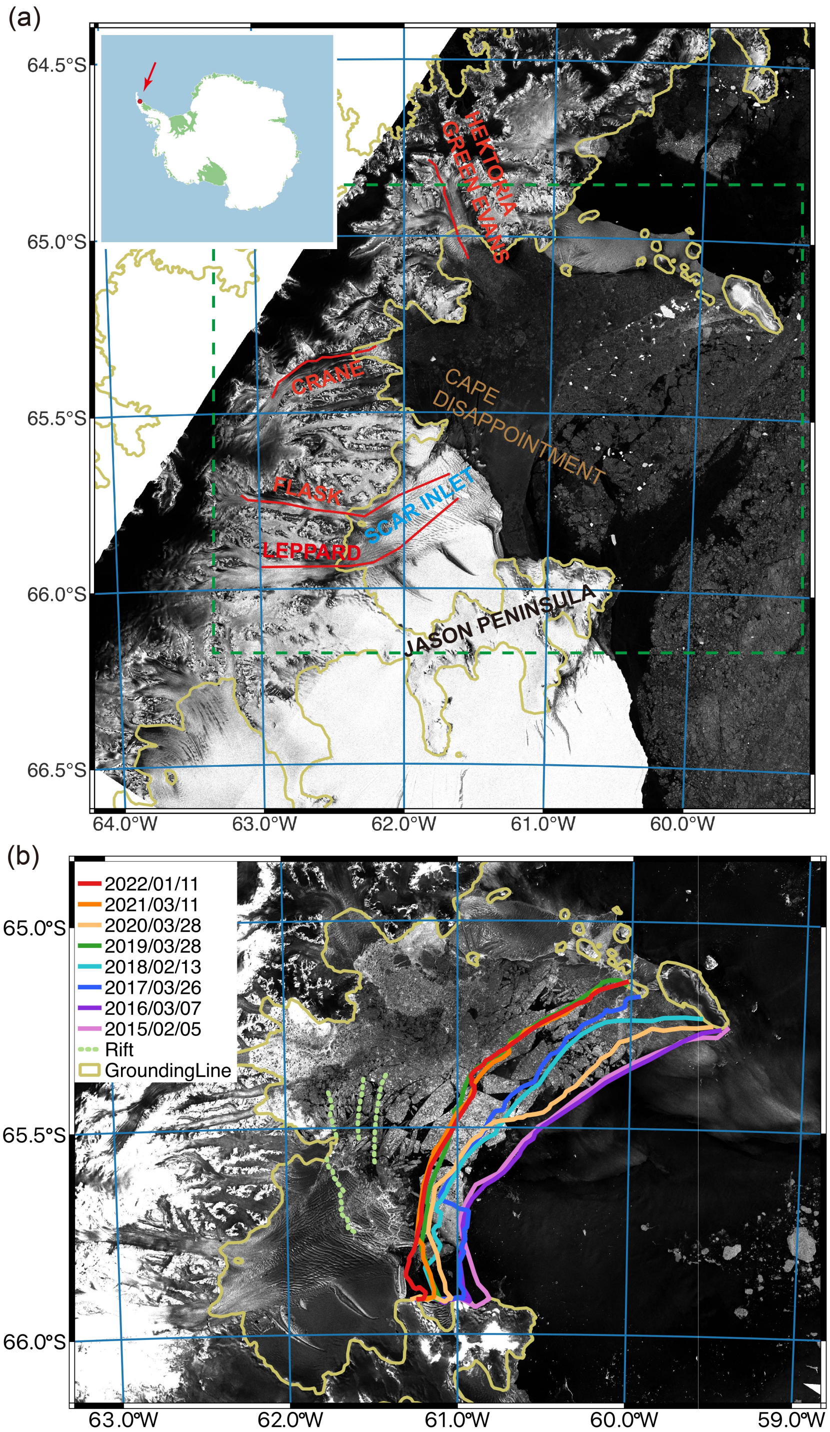

Figure 1. Sentinel-1 SAR amplitude image of the Larsen B area taken on September 30, 2020 (a). SAR image showing collapsed Larsen B landfast ice on January 23, 2022 (b). Yellow lines represent the grounding lines (Rignot et al., 2013; Mouginot et al., 2017). (a) Red lines show the profiles of four glaciers. Red arrow shows the location of our study area in the inserted subfigure. The dark green dash box indicates the approximate region for 1b. (b) Colored lines are the most retreated SLIEs for each year prior to collapse. Light green dashed lines denote the locations of pre-existing rifts.

sea ice, oceans, and the atmosphere. Hydrofracture by surface meltwater (Nye, 1957; Van der Veen, 1998), plate bending by buoyancy forces (Braun & Humbert, 2009; T. Scambos et al., 2009), sea ice loss, ocean swell (Massom et al., 2018), and crevasse-rift system (Glasser & Scambos, 2008; Rack & Rott, 2004) may have caused the disintegration of the Larsen A, B, and Wilkins Ice Shelves. One important observation is the widespread meltwater ponds on the Larsen Ice Shelf before disintegration (van den Broeke, 2005; Sergienko & Macayeal, 2005), possibly related to foehn winds and atmospheric rivers (Cape et al., 2015; Wille et al., 2022). Several models, which consist of densely distributed melt-filled crevasses, have been proposed to explain the cascading collapse of ice shelves into small pieces in a short period (MacAyeal et al., 2003; Banwell et al., 2013; Robel & Banwell, 2019). Meltwater ponding is observed every summer on the Larsen B landfast sea ice from Sentinel-1 SAR, Sentinel-2, and MODIS (Moderate Resolution Imaging Spectroradiometer) images. However, the mechanism for landfast sea ice disintegration may differ from the Larsen B Ice Shelf in 2002 due to different mechanical properties of the sea ice (Timco & Weeks, 2010).

Floating ice, restricted laterally by islands, peninsulas, or grounded icebergs, acts like the neck of an hourglass, slowing down the grounded glaciers flowing to the ocean. This buttressing effect can be quantitatively measured by the stress change at the grounding line after the hypothetical removal of the floating ice (Gudmundsson, 2013). It can also be evaluated by using ice-flow models with data assimilation, from which parameters such as stress and viscosity can be estimated. Fürst et al. (2016) estimated the buttressing potential of ice shelves by modeling the second principal horizontal stress (Doake et al., 1998), while Reese et al. (2018) studied it by calculating ice flux change due to the thinning of a given piece of the ice shelf. In terms of landfast ice, Greene et al. (2018) and Gomez-Fell et al. (2022) suggested that it can also buttress the ice shelves because the velocity of the ice shelves strongly correlates with the thickness or extent of landfast ice. In this paper, we adopt this idea to study the buttressing effect of the landfast sea ice that occupied the Larsen B Embayment from 2011 to 2022.

2 Data and methods

We use repeated acquisitions from Sentinel-1 SAR (Supplementary Movie S1) to obtain the relative displacement of the ice surface using the offset tracking technique in the slant-range and azimuth directions, which are perpendicular and parallel to the flight direction, respectively (Strozzi et al., 2002; Joughin, 2002). Next, we use the predicted tide height in the model CATS2008 to remove vertical tidal motions from range displacements to isolate the horizontal displacements. Finally, we use a median filter to smooth the data in the spatial and temporal domains (see details in Supplementary Text S1 Section 1).

To show a cleaner map of velocity, we use two methods. In the first, we smooth the horizontal velocity maps (Supplementary Movie S2) with a second-order Savitzky–Golay filter (Savitzky & Golay, 1964) with a square window size of about 4 km. In the second method, we fit the velocity time-series in the temporal domain to remove the noise and make Movie S3 (horizontal velocity) using the time-series inversion package "iceutils.tseries" (Riel et al., 2014, 2021), which decomposes the signal into secular, seasonal, and transient terms (see details in Supplementary Text S1 Section 3). Movie S2 has a higher spatial resolution, while Movie S3 is less noisy due to the smoothing inherent in the time-series method. Furthermore, we calculate the strain rate maps (Supplementary Movie S4 and S5) from the horizontal velocity maps (Movie S2). Movies S4 and S5 show horizontal dilation strain rate $\dot{\epsilon}_{dilate}$ (the trace of the horizontal strain rate tensor), maximum shear strain rate $\dot{\epsilon}_{shear}$, strain rate along the flow direction $\dot{\epsilon}_{xx}$, and effective strain rate $\dot{\epsilon}_E$ (the second invariant of 3D strain rate tensor), respectively. These terms are defined in Supplementary Text S1 Section 4. To study the temporal change of landfast ice area, we use the cross-correlation method to find the stationary fast ice that moves less than 100 m within 12 days (see details in Supplementary Text S1 Section 2), and delineate the seaward landfast ice edge (SLIE; colored lines in Figure 1b).

3 Results

3.1 Disintegration of landfast sea ice

A time-series of SAR images (collected from Sentinel-1 Path 38) shows the evolution of ice shelves and sea ice (Movie S1). The Larsen B landfast sea ice collapsed into large pieces by January 23, 2022, later drifting counterclockwise on the ocean. It likely broke up between January 19 and 21, inferred from cloudy Moderate Resolution Imaging Spectroradiometer (MODIS) images from NASA's Terra and Aqua satellites. Melange plumes appeared at the end of most glaciers, where ice fragment size is too small to see with SAR. A piece of the Scar Inlet Ice Shelf, comparable in size to the city of Philadelphia, also broke off in this event. This disintegration is different from the 2002 event when only one giant melange plume was observed (Massom et al., 2018). This difference may be due to the sea ice pieces being too thin (Fraser et al., 2021) and too areally extensive to cause fragments to capsize (MacAyeal et al., 2003). After the disintegration, the Hektoria-Green-Evans Glacier retreated and lost about 200 square kilometers in late March (Movie S1).

The sea ice in Antarctica reached a new record low in 2022, probably due to a warmer ocean and strong winds (Raphael & Handcock, 2022). MODIS observed widespread meltwater ponds on the fast ice before disintegration. We investigate the locations of the SLIE every year when the landfast ice extent is the smallest (Figure 1b), which generally retreats landward over the years except 2020. The landfast ice extent reached one of the lowest points just before the collapse in January 2022. The south end of SLIE retreated to the grounded ice (pinning point) near the Jason Peninsula, which also broke off later. Meanwhile, the Philadelphia-size iceberg calved along the opening rift on the Scar Inlet Ice Shelf (green dashed line in Figure 1b). Most broken sea ice pieces near the Cape Disappointment are long and thin rectangles aligned in a similar direction as the rifts. Therefore, we suggest that the four opening rifts we identified in Section 3.3 may contribute to the collapse of the whole landfast ice.

3.2 Landfast sea ice buttressing

This collapsing event provides an opportunity to study the buttressing effect of the landfast sea ice. Some glaciers accelerated up to eightfold about nine months after the collapse of Larsen B Ice Shelf in 2002 (Rignot et al., 2004; T. A. Scambos et al., 2004; Wuite et al., 2015), but it remains unclear whether the sea ice provides enough buttressing stress to meaningfully slow down glaciers. Acceleration of upstream glaciers after the removal of landfast sea ice would show that landfast sea ice in the Larsen B embayment can generate sufficiently high resistive stresses to slow the flow of glaciers. However, the eight months of observations along profiles on four glaciers, which are similar locations as Rignot et al. (2004) (cf. their Figure 3) after the collapse, show no increase in speed (our Figure 2). The speed increase downstream of Hektoria-Green-Evans Glaciers in April (orange dots in Figure 2a) actually reflects the melange plume's speed after the breakup (see details in Movie S1). Because our post-collapse observation time scale spans only eight months, we also analyze the horizontal velocity time-series before the collapse to study its relation with the landfast sea ice extent and buttressing effect.

Figure 3a and Movie S3 illustrate the evolution of velocity, the average of which is about $2 - 3$ m/day in the Larsen B region and increases toward the seaward front. To extract the meaningful signals from the velocity time-series (dots in Figure 3d), we use the inversion method (Riel et al., 2014, 2021) to fit the curves (solid lines). Figure 3d shows a small seasonal variation of velocity for the grounded glacier (red line; A in

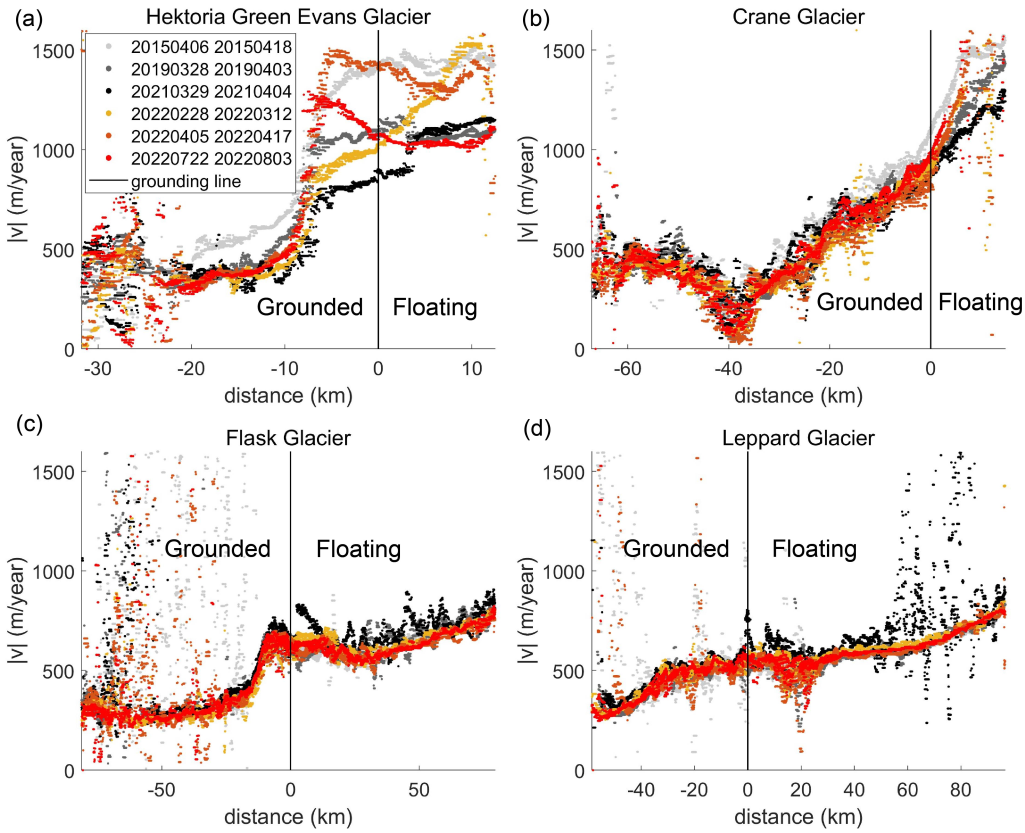

Figure 2. Speed along the profiles (red lines in Figure 1a) for four glaciers. The distance is relative to where the transect crosses the grounding line, with positive values being downstream on the floating ice. Different colors represent pairs for different times (format: yyyymmdd; before collapse: white, gray, and black; after collapse: yellow, orange, and red).

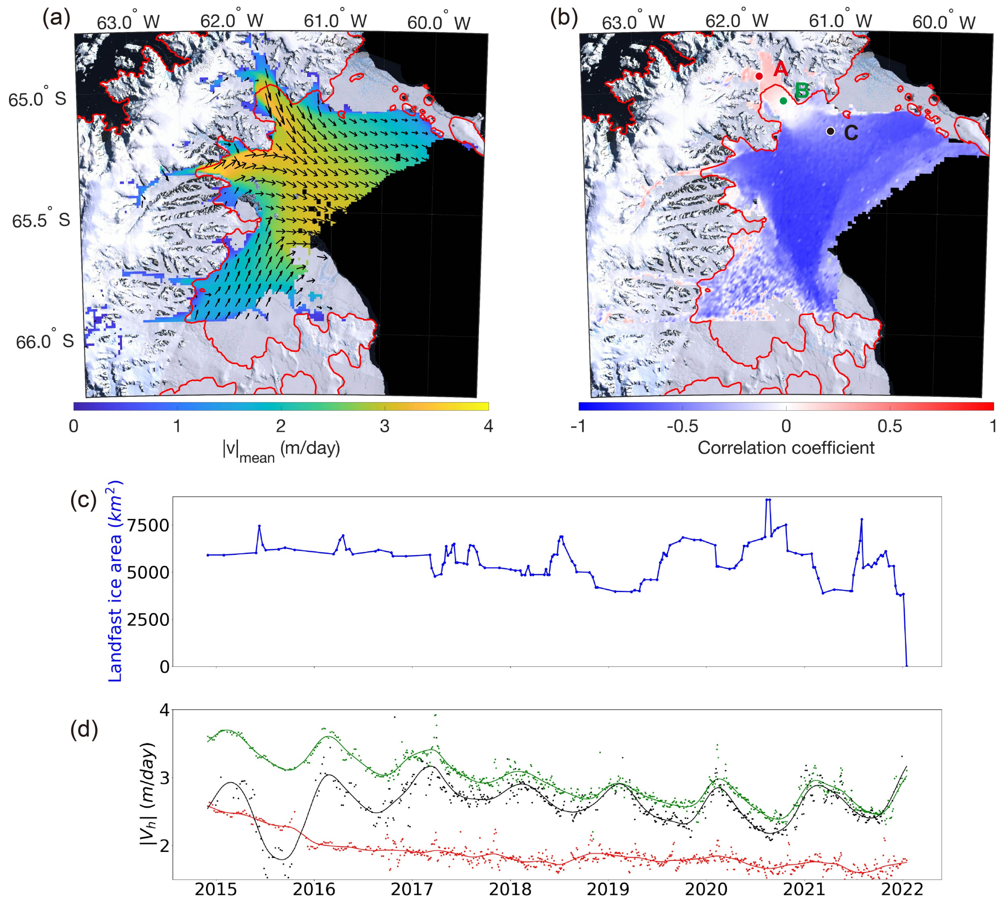

Figure 3. Horizontal velocity after time-series curve fitting and its relation with landfast ice extent. (a) The average horizontal velocity map of Larsen B embayment represented by both the colorbar and vectors. (b) The map of correlation coefficient between speed and landfast sea ice extent. (c) Evolution of the landfast sea ice extent. (d) Time-series of horizontal speed (dots) and fitting lines at 3 locations denoted by dots (Figure 3b). The red lines show the grounding lines and the background map is the Landsat Image Mosaic of Antarctica (Bindschadler et al., 2008) (Figure 3a and b).

Figure 3b). In contrast, the seasonal variation gets larger downstream on the landfast sea ice (green and black lines; B and C in Figure 3b).

To evaluate the buttressing effect, we calculate the correlation coefficient between the landfast sea ice area (Figure 3c) and horizontal velocity. Sea ice adheres to the landfast sea ice, and its area gets larger in winter, while ice breaks away to reduce the areal extent in the summer (Movie S1). The landfast sea ice velocity shown in Figure 3d is higher in summer and lower in winter, so the correlation coefficient is generally negative. Buttressing stress comes from the confined margin of landfast ice with ice shelves, land, or islands (Gudmundsson, 2013; Schoof, 2007). Therefore, it should increase with the contact area between the ice and the solid Earth. We take the areal extent of the sea ice as a proxy for this contact area. Thus, if the velocity variation of the upstream glaciers negatively correlates with the extent of the landfast sea ice, the sea ice has a “tele-buttressing” effect, as discussed in Reese et al. (2018). We use a fitting curve from time-series inversion (Supplementary Text S1 Section 3) to do the correlation because the high-frequency signals (with periods shorter than 10 days) are removed, giving a similar sampling rate to the fast ice extent data.

We show correlation coefficients for every location where velocity data are available more than 50% of the time (Figure 3b). The correlation coefficient is negative on the landfast sea ice, while it is near 0 on the glacier outlets and slightly below 0 on the Scar Inlet Ice Shelf. The slight positive correlation on the Hecktoria-Green-Evans glacier is due to the decreasing trend of velocity (Figure 3d). Our results suggest that the buttressing stress from the Larsen B landfast sea ice may not transmit to the upstream glaciers due to a combination of thinner ice with different mechanical properties and materials damaged from the previous long-lived ice shelves (Domack et al., 2005). This result agrees with the observation of no speed-up after the removal. At this time, it is not clear how to estimate the relative importance of buttressing of ice thickness and differing mechanical properties between the sea ice pack and the Larsen B Ice Shelf, only to say that the sea ice pack provided little buttressing relative to the ice shelf.

3.3 Rift and pressure ridge

The SLIE in Larsen B usually retreats from autumn to winter and advances from spring to summer (blue line in Figure 3c). To study these processes and corresponding rifts and pressure ridges, we take the gradient of the spatially-smoothed velocity field to produce the strain maps (Movie S4 and S5; method discussed in Text S1 Section 4). The strain-rate maps ($\dot{\epsilon}_{dilate}$ in Movie S4) show high compressional strain rates (blue) at the boundary when the drift ice sticks to the landfast ice. This signal indicates the formation of the pressure ridge (Feltham, 2008), which originates from the collision of two pieces of ice driven by wind or ocean currents. We also observe rifts with a high extensional strain rate (red) several days before a piece of ice breaks away from the landfast ice in Movie S4. Therefore, we can consider this phenomenon as a precursor to the ice-calving event.

We show two cases with rifts and pressure ridges inside the landfast sea ice in Figure 4. First, pressure ridges (in blue) showed up at the downstream landfast sea ice of the Hektoria, Crane Glaciers, and Scar Inlet Ice Shelf from June to September in 2015 (Figure 4a). This event happened when the upstream glaciers accelerated (red dots in Figure 3d), so the downstream landfast ice was in compression. If the sea ice is mechanically strong and coherent, there will be a widespread slightly-compressed zone. Therefore, the localized compressional arches indicate that sea ice deforms plastically, and stress becomes independent of strain when it exceeds a certain yield criterion. We suggest this is because sea ice is porous and has low cohesion (Timco & Weeks, 2010; Feltham, 2008; Hibler, 1979).

Second, Figure 4d shows three rifts near Cape Disappointment and one on the Scar Inlet Ice shelf, which emerged during the observation period and probably caused the collapse of the whole landfast sea ice pack (also marked as green dashed lines in Figure 1b). Movie S4 shows that the dilatation strain rate in these rifts is positive continuously, which means they opened plastically after they fractured. The western rift on the landfast sea ice connects with the rift on the ice shelf, which suggests the landfast ice mechanically couples with the ice shelf to some extent. Three opening rifts fractured because the northeast-moving Scar Inlet Ice Shelf protruded into the landfast ice, and it pulled apart the landfast sea ice on the northern side (see velocity directions in Figure 3a). The rift on the front of the Scar Inlet Ice Shelf ruptured because the east-moving landfast ice sheared the indented piece, and the ice shelf was also in an extensional environment. Therefore, these observations suggest that the relative motions of the landfast ice and ice shelf are mainly responsible for the formation of the rifts.

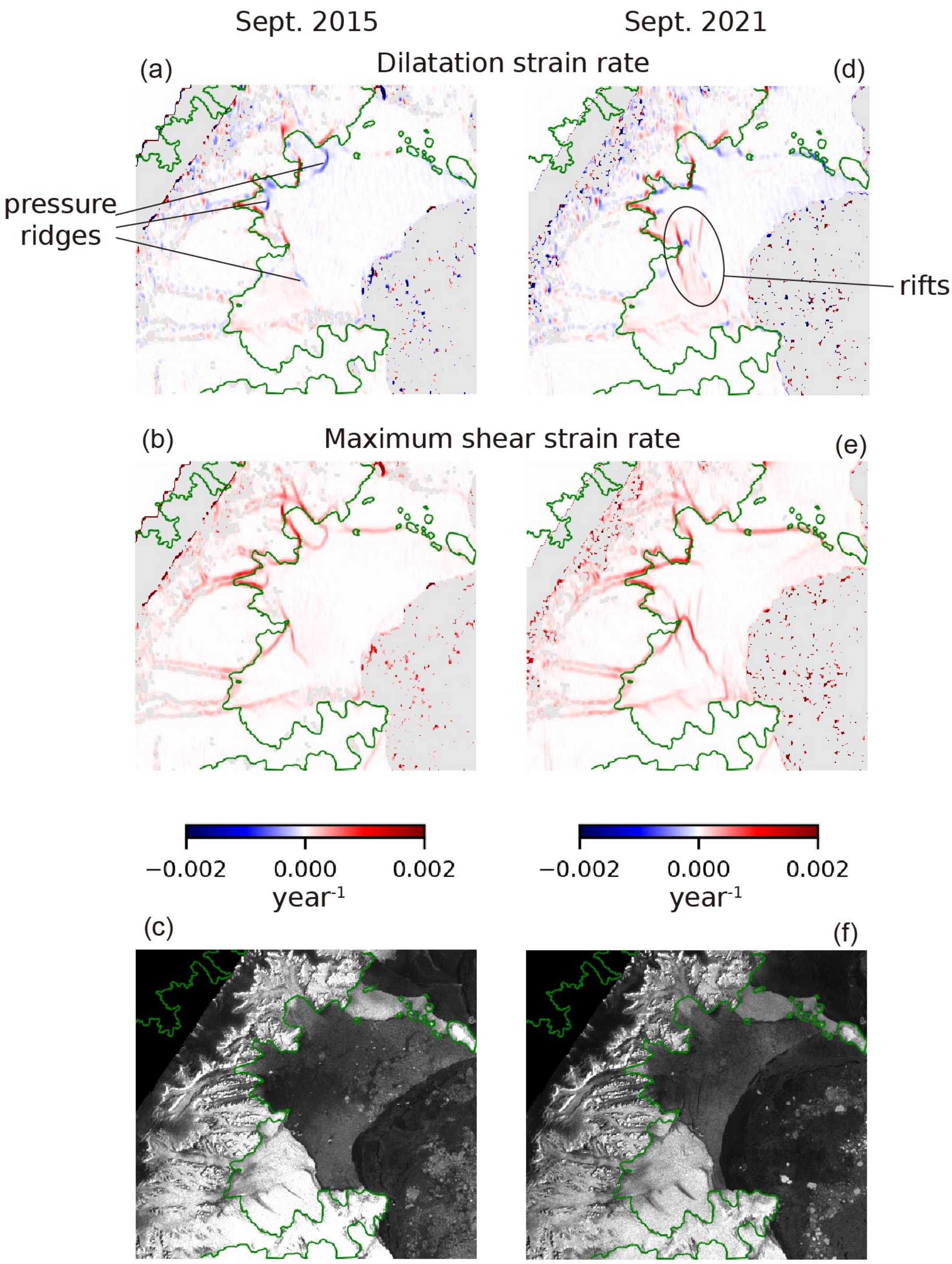

Figure 4. The dialation strain rate $\dot{\epsilon}_{dilate}$, shear strain rate $\dot{\epsilon}_{shear}$ and SAR images in 2015 (a-c) and 2021 (b-f). The strain rate maps represent the deformation between Sept. 9 and Sept. 21, 2015 (a, b), and between Sept. 13 and Sept. 19, 2021 (d, e), respectively. The SAR intensity images are taken on Sept. 21, 2015, and Sept. 19, 2021, respectively. Red represents extension while blue represents compression for the $\dot{\epsilon}_{dilate}$ maps (a, d). Green lines indicate the grounding lines.

4 Discussion and conclusion

The horizontal velocity fields derived from SAR data provide multiple lines of evidence showing that the sea ice pack that filled the Larsen B embayment from 2014 to 2022 provided little buttressing to the grounded glaciers. We find no glacier acceleration after fast ice disintegration and no correlation between glacier velocity and landfast sea ice extent. This is because fast ice is thinner and weaker than the ice shelf that filled the embayment prior to 2002. These characteristics cause landfast sea ice to readily develop large-scale damage features, including the pressure ridges and opening rifts we observe, which reduce the sea ice pack's ability to provide buttressing stresses.

Our argument of negligible buttressing from the sea ice pack is supported by the absence of observable glacier acceleration in the first eight months following the collapse of the ice pack. This result differs from observations following the collapse of the Larsen B Ice Shelf that showed a significant velocity increase on the Crane and Hektoria-Green-Evans Glaciers one year after the collapse (Rignot et al., 2004). We attribute this difference to the fact that the Larsen B Ice Shelf was much thicker and likely more competent at the time of its collapse than the sea ice pack, which allowed the ice shelf to support higher buttressing stresses.

The second piece of evidence is that we find no negative correlation between fast ice extent and velocity on the glaciers. Specifically, the seasonal fluctuation of horizontal velocity is large on the fast ice but is negligibly small on the grounded glaciers and the Scar Inlet Ice Shelf. In contrast, Greene et al. (2018) and Gomez-Fell et al. (2022) found a good correlation between sea ice extent and ice shelf velocity in other areas, probably because their study areas have different geographical locations relative to the ocean and land. For example, the Parker Ice Tongue studied in Gomez-Fell et al. (2022) protrudes into the surrounding sea ice and is thus more sensitive to changes in buttressing at the calving front. Furthermore, the difference between those studies and ours is due to the fact that we also focus on grounded glaciers, which have additional basal drag to resist changes in flow.

We observe the formation of four opening rifts from the strain rate maps (Figure 4d), which may contribute to the disintegration of the whole landfast sea ice. They are much longer than that found on the previous Larsen B Ice Shelf (Glasser & Scambos, 2008), which can undermine the structural integrity of the sea ice pack, further leading to its collapse. We also observe that the fast ice collapsed differently from the ice shelf collapse in 2002. A large melange plume was observed after the collapse in 2002, but the landfast sea ice broke up into large pieces, which implies that sea ice is too thin to capsize and cannot break up in a cascade.

Taken together, the decade-long observations of the Larsen B embayment show that the landfast sea ice that occupied the same area as the Larsen B Ice Shelf did not provide the same buttressing stress as the previous ice shelf, suggesting that if more ice shelves collapse due to climate change, the upstream glaciers will likely accelerate regardless of sea ice conditions. In other words, this finding suggests that ice shelf buttressing is not renewable over sub-decadal timescales. Our observations also elucidate ice-ocean-atmosphere interaction and help to monitor sea-ice-related hazards. For instance, the shrinking landfast sea ice and the large seasonal variation of its horizontal velocity we observe have the potential to illuminate how the ocean and climate influence ice evolution. In addition, the transient signals of high strain rates can be used as precursors for calving events or massive ice collapses.

Open Research Section

We use Copernicus Sentinel-1 synthetic SAR data from 2014 to 2022, retrieved from ASF DAAC and processed by ESA (`https://search.asf.alaska.edu/`). We use the

InSAR Scientific Computing Environment ISCE (Rosen et al., 2012) to perform the pixel offset tracking (`https://github.com/isce-framework`). The tide model CATS2008 (Padman et al., 2002, 2008) for tide correction is available at `https://www.esr.org/research/polar-tide-models/list-of-polar-tide-models/cats2008/`. The software "iceutils" (Riel et al., 2014, 2021) for filtering and strain rate calculation is available at `https://github.com/bryanvriel/iceutils`. We use the software "hyp3_timeseries" (`https://github.com/jlinick/hyp3_timeseries`) to make Supplementary Movie S1. We use the QGIS (`https://qgis.org/en/site/forusers/download.html`) and Qantarctica software (`https://www.npolar.no/quantarctica/`) to plot Figure 1. Our final data products, including velocity and strain rate fields used in Movie S2-S5, are archived in Zenodo (`https://doi.org/10.5281/zenodo.7818543`).

Acknowledgments

The authors thank Camilla Cattania, Justin Linick, Colin Meyer, Enrico Milanese, Joanna Millstein, Meghana Ranganathan, and Sarah Wells-Moran for helpful discussions. Y.S. received fundings from MIT EAPS Robert R Shrock Fellowship, Sven Treitel (1953) Fellowship, and MIT Mathworks Fellowship. B.M. and B.R. received funding from NSFGEO-NERC grant 1853918, the John W. Jarve (1978) Seed Fund for Science Innovation, and the Earl A Killian III (1978) and Waidy Lee Fund.

References

Armstrong, T. (1972). World meteorological organization. wmo sea-ice nomenclature. terminology, codes and illustrated glossary. edition 1970. geneva, secretariat of the world meteorological organization, 1970.[ix], 147 p.[including 175 photos]+ corrigenda slip.(wmo/omm/bmo, no. 259, tp. 145.). *Journal of Glaciology*, *11*(61), 148–149.

Banwell, A. F., MacAyeal, D. R., & Sergienko, O. V. (2013). Breakup of the larsen b ice shelf triggered by chain reaction drainage of supraglacial lakes. *Geophysical Research Letters*, *40*(22), 5872–5876.

Bindschadler, R. (2006). Hitting the ice sheets where it hurts. *Science*, *311*(5768), 1720–1721.

Bindschadler, R., Vornberger, P., Fleming, A., Fox, A., Mullins, J., Binnie, D., ... Gorodetzky, D. (2008). The landsat image mosaic of antarctica. *Remote Sensing of Environment*, *112*(12), 4214–4226.

Braun, M., & Humbert, A. (2009). Recent retreat of wilkins ice shelf reveals new insights in ice shelf breakup mechanisms. *IEEE Geoscience and Remote Sensing Letters*, *6*(2), 263–267.

Cape, M., Vernet, M., Skvarca, P., Marinsek, S., Scambos, T., & Domack, E. (2015). Foehn winds link climate-driven warming to ice shelf evolution in antarctica. *Journal of Geophysical Research: Atmospheres*, *120*(21), 11–037.

De Angelis, H., & Skvarca, P. (2003). Glacier surge after ice shelf collapse. *Science*, *299*(5612), 1560–1562.

DeConto, R. M., & Pollard, D. (2016). Contribution of antarctica to past and future sea-level rise. *Nature*, *531*(7596), 591–597.

Depoorter, M. A., Bamber, J. L., Griggs, J. A., Lenaerts, J. T., Ligtenberg, S. R., van den Broeke, M. R., & Moholdt, G. (2013). Calving fluxes and basal melt rates of antarctic ice shelves. *Nature*, *502*(7469), 89–92.

Doake, C., Corr, H., Rott, H., Skvarca, P., & Young, N. (1998). Breakup and conditions for stability of the northern larsen ice shelf, antarctica. *Nature*, *391*(6669), 778–780.

Domack, E., Duran, D., Leventer, A., Ishman, S., Doane, S., McCallum, S., ... Prentice, M. (2005). Stability of the larsen b ice shelf on the antarctic peninsula during the holocene epoch. *Nature*, *436*(7051), 681–685.

Dupont, T., & Alley, R. (2005). Assessment of the importance of ice-shelf buttressing to ice-sheet flow. *Geophysical Research Letters*, *32*(4).

Feltham, D. L. (2008). Sea ice rheology. *Annu. Rev. Fluid Mech.*, *40*, 91–112.

Fraser, A. D., Massom, R. A., Handcock, M. S., Reid, P., Ohshima, K. I., Raphael, M. N., ... Porter-Smith, R. (2021). Eighteen-year record of circum-antarctic landfast-sea-ice distribution allows detailed baseline characterisation and reveals trends and variability. *The Cryosphere*, *15*(11), 5061–5077.

Fürst, J. J., Durand, G., Gillet-Chaulet, F., Tavard, L., Rankl, M., Braun, M., & Gagliardini, O. (2016). The safety band of antarctic ice shelves. *Nature Climate Change*, *6*(5), 479–482.

Glasser, N., & Scambos, T. A. (2008). A structural glaciological analysis of the 2002 larsen b ice-shelf collapse. *Journal of Glaciology*, *54*(184), 3–16.

Gomez-Fell, R., Rack, W., Purdie, H., & Marsh, O. (2022). Parker ice tongue collapse, antarctica, triggered by loss of stabilizing land-fast sea ice. *Geophysical Research Letters*, *49*(1), e2021GL096156.

Greene, C. A., Young, D. A., Gwyther, D. E., Galton-Fenzi, B. K., & Blankenship, D. D. (2018). Seasonal dynamics of totten ice shelf controlled by sea ice buttressing. *The Cryosphere*, *12*(9), 2869–2882.

Gudmundsson, G. (2013). Ice-shelf buttressing and the stability of marine ice sheets. *The Cryosphere*, *7*(2), 647–655.

Hibler, W. D. (1979). A dynamic thermodynamic sea ice model. *Journal of physical oceanography*, *9*(4), 815–846.

Joughin, I. (2002). Ice-sheet velocity mapping: a combined interferometric and speckle-tracking approach. *Annals of Glaciology*, *34*, 195–201.

Lai, C.-Y., Kingslake, J., Wearing, M. G., Chen, P.-H. C., Gentine, P., Li, H., … van Wessem, J. M. (2020). Vulnerability of antarctica's ice shelves to meltwater-driven fracture. *Nature*, *584*(7822), 574–578.

Lenaerts, J., Lhermitte, S., Drews, R., Ligtenberg, S., Berger, S., Helm, V., … others (2017). Meltwater produced by wind–albedo interaction stored in an east antarctic ice shelf. *Nature climate change*, *7*(1), 58–62.

MacAyeal, D. R., Scambos, T. A., Hulbe, C. L., & Fahnestock, M. A. (2003). Catastrophic ice-shelf break-up by an ice-shelf-fragment-capsize mechanism. *Journal of Glaciology*, *49*(164), 22–36.

Massom, R. A., Scambos, T. A., Bennetts, L. G., Reid, P., Squire, V. A., & Stammerjohn, S. E. (2018). Antarctic ice shelf disintegration triggered by sea ice loss and ocean swell. *Nature*, *558*(7710), 383–389.

Mercer, J. H. (1978). West antarctic ice sheet and co2 greenhouse effect: a threat of disaster. *Nature*, *271*(5643), 321–325.

Mouginot, J., Scheuchl, B., & Rignot, E. (2017). Measures antarctic boundaries for ipy 2007–2009 from satellite radar, version 2. *National Snow and Ice Data Center*, *10*.

Nye, J. F. (1957). The distribution of stress and velocity in glaciers and ice-sheets. *Proceedings of the Royal Society of London. Series A. Mathematical and Physical Sciences*, *239*(1216), 113–133.

Padman, L., Erofeeva, S. Y., & Fricker, H. A. (2008). Improving antarctic tide models by assimilation of icesat laser altimetry over ice shelves. *Geophysical Research Letters*, *35*(22).

Padman, L., Fricker, H. A., Coleman, R., Howard, S., & Erofeeva, L. (2002). A new tide model for the antarctic ice shelves and seas. *Annals of Glaciology*, *34*, 247–254.

Pritchard, H., Ligtenberg, S. R., Fricker, H. A., Vaughan, D. G., van den Broeke, M. R., & Padman, L. (2012). Antarctic ice-sheet loss driven by basal melting of ice shelves. *Nature*, *484*(7395), 502–505.

Rack, W., & Rott, H. (2004). Pattern of retreat and disintegration of the larsen b ice shelf, antarctic peninsula. *Annals of glaciology*, *39*, 505–510.

Raphael, M. N., & Handcock, M. S. (2022). A new record minimum for antarctic sea ice. *Nature Reviews Earth & Environment*, 1–2.

Reese, R., Gudmundsson, G. H., Levermann, A., & Winkelmann, R. (2018). The far reach of ice-shelf thinning in antarctica. *Nature Climate Change*, *8*(1), 53–57.

Riel, B., Minchew, B., & Joughin, I. (2021). Observing traveling waves in glaciers with remote sensing: new flexible time series methods and application to sermeq kujalleq (jakobshavn isbræ), greenland. *The Cryosphere*, *15*(1), 407–429.

Riel, B., Simons, M., Agram, P., & Zhan, Z. (2014). Detecting transient signals in geodetic time series using sparse estimation techniques. *Journal of Geophysical Research: Solid Earth*, *119*(6), 5140–5160.

Rignot, E., Casassa, G., Gogineni, P., Krabill, W., Rivera, A., & Thomas, R. (2004). Accelerated ice discharge from the antarctic peninsula following the collapse of larsen b ice shelf. *Geophysical research letters*, *31*(18).

Rignot, E., Jacobs, S., Mouginot, J., & Scheuchl, B. (2013). Ice-shelf melting around antarctica. *Science*, *341*(6143), 266–270.

Robel, A. A., & Banwell, A. F. (2019). A speed limit on ice shelf collapse through hydrofracture. *Geophysical Research Letters*, *46*(21), 12092–12100.

Rosen, P. A., Gurrola, E., Sacco, G. F., & Zebker, H. (2012). The insar scientific computing environment. In *Eusar 2012; 9th european conference on synthetic aperture radar* (pp. 730–733).

Savitzky, A., & Golay, M. J. (1964). Smoothing and differentiation of data by simplified least squares procedures. *Analytical chemistry*, *36*(8), 1627–1639.

Scambos, T., Fricker, H. A., Liu, C.-C., Bohlander, J., Fastook, J., Sargent, A., ... Wu, A.-M. (2009). Ice shelf disintegration by plate bending and hydro-fracture: Satellite observations and model results of the 2008 wilkins ice shelf break-ups. *Earth and Planetary Science Letters*, *280*(1-4), 51–60.

Scambos, T. A., Bohlander, J., Shuman, C. A., & Skvarca, P. (2004). Glacier acceleration and thinning after ice shelf collapse in the larsen b embayment, antarctica. *Geophysical Research Letters*, *31*(18).

Schoof, C. (2007). Ice sheet grounding line dynamics: Steady states, stability, and hysteresis. *Journal of Geophysical Research: Earth Surface*, *112*(F3).

Sergienko, O., & Macayeal, D. R. (2005). Surface melting on larsen ice shelf, antarctica. *Annals of Glaciology*, *40*, 215–218.

Shepherd, A., Wingham, D., & Rignot, E. (2004). Warm ocean is eroding west antarctic ice sheet. *Geophysical Research Letters*, *31*(23).

Strozzi, T., Luckman, A., Murray, T., Wegmuller, U., & Werner, C. L. (2002). Glacier motion estimation using sar offset-tracking procedures. *IEEE Transactions on Geoscience and Remote Sensing*, *40*(11), 2384–2391.

Timco, G., & Weeks, W. (2010). A review of the engineering properties of sea ice. *Cold regions science and technology*, *60*(2), 107–129.

van den Broeke, M. (2005). Strong surface melting preceded collapse of antarctic peninsula ice shelf. *Geophysical Research Letters*, *32*(12).

Van der Veen, C. (1998). Fracture mechanics approach to penetration of surface crevasses on glaciers. *Cold Regions Science and Technology*, *27*(1), 31–47.

Wille, J. D., Favier, V., Jourdain, N. C., Kittel, C., Turton, J. V., Agosta, C., ... others (2022). Intense atmospheric rivers can weaken ice shelf stability at the antarctic peninsula. *Communications Earth & Environment*, *3*(1), 1–14.

Wuite, J., Rott, H., Hetzenecker, M., Floricioiu, D., De Rydt, J., Gudmundsson, G., ... Kern, M. (2015). Evolution of surface velocities and ice discharge of larsen b outlet glaciers from 1995 to 2013. *The Cryosphere*, *9*(3), 957–969.

Supporting Information for "Disintegration and Buttressing Effect of the Landfast Sea Ice in the Larsen B Embayment, Antarctic Peninsula"

Yudong Sun[1], Bryan Riel[1,2]and Brent Minchew[1]

[1]Department of Earth, Atmospheric, and Planetary Sciences, Massachusetts Institute of Technology, Cambridge, MA, USA

[2]School of Earth Sciences, Zhejiang University, Hangzhou, Zhejiang, China

Contents of this file

1. Text S1
2. Figures S1 to S2

Additional Supporting Information (Files uploaded separately)

1. Captions for Movies S1 to S5

Introduction

The Supplementary Material consists of the following parts:

Supplementary text S1 describes data and methods for pixel offset tracking, filtering, measuring fast ice extent, and calculating strain rate.

Figure S1 compares velocity data before and after tide correction and median filtering.

Figure S2 shows time-series inversion for velocity curve fitting and its "L-curve".

Movie S1 is a SAR movie.

Movie S2 and S3 are horizontal velocity maps with different filtering.

Movie S4 and S5 are the strain rate maps.

High-resolution movies can be found at:

`https://drive.google.com/drive/folders/1OSnWMyDJBEQifgNMruqSgHdfDu8QQbzb?usp=share_link`

Text S1. Data and methods

1. SAR pixel offset tracking

SAR data We use C-band Copernicus Sentinel-1 synthetic aperture radar (SAR) data from 2014 to 2022, retrieved from ASF DAAC and processed by ESA. We use the software "hyp3_timeseries" (`https://github.com/jlinick/hyp3_timeseries`) to make a time-lapse SAR movie (Supplementary Movie S1). Sentinel-1A and Sentinel-1B have a 12-day revisit period, so the shortest interval is 6 days if our area is visited by one satellite and followed by the other. We use the interferometric wide swath Single-Look-Complex (SLC) products on a descending track (path 38) with a platform heading direction of about 23° to the west of south. The incidence angles for three swaths are 32.9°, 38.3°, and 43.1°, and the pixel size is 2.3×14.1 m in the range and azimuth directions.

Pixel offset tracking We calculate near-instantaneous velocity on the glacier surface from the relative displacement during the revisit interval, 6 and 12 days. The displacement of a specific ground target can be measured by comparing the offset between the pixel locations of that target from two co-registered SAR images. The pixel offset tracking technique involves applying a two-dimensional cross-correlation operation between multiple image patches of finite size between the reference and secondary images. Each cross-correlation operation results in a correlation surface, and the location of the peak of that surface is proportional to the displacement between the image patches. We slide a patch with a finite size (256×64 pixels) to do the cross-correlation with a search window size as 40×10 pixels. In this way, we create a dense offset map with a skip width and height between patches as 128 and 32 pixels. Therefore, the maximum velocity we can measure is about 7.7 m/day if the time interval is 12 days. The precision of pixel offset tracking is about one-tenth of the pixel size, so the speed error is about 0.24 m/day for a 6-day interval (Strozzi et al., 2002). We use the InSAR Scientific Computing Environment ISCE (Rosen et al., 2012) to perform the pixel offset tracking. In order to do the stack processing, which produces a stack of precisely co-registered SAR images, we use the "topsStack" package implemented in the ISCE environment (Fattahi et al., 2016). The topography model used for co-registration and removal of processing artifacts is the Reference Elevation Model of Antarctica REMA (Howat et al., 2019).

Tide correction We use the tide model CATS2008 (Padman et al., 2002, 2008), to infer the displacements in the horizontal plane. Because we are measuring three-dimensional motion with only two-components of observations (slant-range and azimuth), we cannot uniquely recover the horizontal motion. Therefore, we utilize the CATS2008 tide model to reduce our degrees of freedom by one. The horizontal range displacement d_{rh} is given by

$$d_{rh} = \frac{d_r + z\cos\theta}{\sin\theta}, \tag{1}$$

where d_r, z, and θ are range displacement, vertical tide displacement, and incidence angle of the satellite, respectively. d_{rh} (blue dots) is compared with $d_r/\sin\theta$ (red dots) and the former has a lower deviation in Figure S1.

Filtering We process the displacement fields with a median filter because they are noisy where the coherence is low. Coherence is the magnitude of complex correlation between two SAR images. For example, the coherence for the landfast sea ice is low in summer when the surface ice melts and changes the scattering geometry (Strozzi et al., 1999). First, we smooth data in the space and time domain by the median filter (blue line in Figure S1) with window sizes about 0.7×0.7 km and 12 days, which reduces the noise and does not smear the fine structures of shear zones. Second, we mask the data with high spatial and temporal gradients to remove the noisy areas such as oceans and areas with surface melting.

2. Fast ice extent

We measure the landfast sea ice extent to study its evolution and relationship with upstream glaciers. The landfast ice is suggested to be defined as the ice pack attached to the coast and remaining still for 20 days (Mahoney et al., 2006). SAR is often used to study the landfast ice because SAR comes from active microwave sensors that can image in day or night conditions and whose long (microwave) wavelengths effectively penetrate cloud cover. Mahoney, Eicken, Graves, Shapiro, and Cotter (2004) identify landfast ice by calculating the difference in spatial gradients between SAR images, while Giles, Massom, and Lytle (2008) use cross-correlation methods to find the stationary fast ice that has a low offset. We choose the second method to delineate the seaward landfast ice edge (SLIE) and use the coastline (Mouginot et al., 2017) and SLIE to estimate the area of the landfast ice. Specifically, we identify the landfast ice that moves less than 100 m within 12 days.

3. Time-series inversion

We fit the time-series velocity curve of a given location on ice shelves or landfast sea ice (Movie S3) to study the temporal change and its controlling factors. The time-series signal is decomposed into secular, seasonal, and transient terms. We use the time series inversion package "iceutils.tseries" (Riel et al., 2014, 2021) to do the regression problem as $Gm = d$, where matrix G consists of the temporal basis functions we use to construct the time-series signal, and m and d are the model and data vectors. We get the unique solution to minimize the cost function ϕ as $\phi = ||Gm - d||_2^2 + \lambda||m||_{1,2}$, using L1-norm or L2-norm regularization with a penalty parameter λ.

The dictionary G includes a linear function, sinusoidal functions with periods of 0.5 and 1 year, and integrated B-splines, which are smooth step functions, with different time scales from 10 to 640 days (Hetland et al., 2012). We repeat the inversion with different penalty parameters λ and construct the L-curve, which illustrates the data misfit versus the norm of the coefficient vector, to choose the "best" λ and determine the degree of overfitting (e.g. Figure S2). We select the value for λ roughly at the corner of the L-curve, 0.1 for L2-norm (ridge regression), and 0.03 for L1-norm regularization (lasso regression).

4. Strain rate map

Strain rate maps are helpful to illustrate the shear bands and rifts, and evaluate the stress state of the ice. We derive the horizontal strain rate tensor $\dot{\boldsymbol{\epsilon}}$ from the velocity field as follows

$$\dot{\boldsymbol{\epsilon}} = \begin{pmatrix} \dot{\epsilon}_{xx} & \dot{\epsilon}_{xy} \\ \dot{\epsilon}_{yx} & \dot{\epsilon}_{yy} \end{pmatrix} = \begin{pmatrix} \frac{\partial U}{\partial x} & \frac{1}{2}\left(\frac{\partial U}{\partial y} + \frac{\partial V}{\partial x}\right) \\ \frac{1}{2}\left(\frac{\partial U}{\partial y} + \frac{\partial V}{\partial x}\right) & \frac{\partial V}{\partial y} \end{pmatrix}, \tag{2}$$

where U and V are horizontal velocity in x and y directions. The dilation strain rate $\dot{\epsilon}_{dilate}$ in the horizontal plane is

$$\dot{\epsilon}_{dilate} = \dot{\epsilon}_{xx} + \dot{\epsilon}_{yy}, \tag{3}$$

where we adopt the convention that $\dot{\epsilon}_{dilate}$ is positive in tension. If we assume that ice is incompressible ($\dot{\epsilon}_{xx}+\dot{\epsilon}_{yy}+\dot{\epsilon}_{zz}=0$), we have $\dot{\epsilon}_{zz}=-\dot{\epsilon}_{dilate}$, indicating that the value of the dilatant strain rate is independent of our choices for the horizontal coordinates x and y. In other words, the incompressibility of ice directly uniquely relates to the dilatant strain rate to the first invariant (*i.e.* trace) of the 3D strain rate tensor. The maximum shear strain rate $\dot{\epsilon}_{shear}$ is similarly invariant to the horizontal coordinate system and is defined as

$$\dot{\epsilon}_{shear}=\sqrt{\frac{1}{4}(\dot{\epsilon}_{xx}+\dot{\epsilon}_{yy})^2+\dot{\epsilon}_{yx}^2-\dot{\epsilon}_{xx}\dot{\epsilon}_{yy}}, \tag{4}$$

as suggested by Nye (1959) and Harper, Humphrey, and Pfeffer (1998). This formulation is equivalent to one-half the difference in the maximum and minimum principal strain rates. The effective strain rate $\dot{\epsilon}_E$, which is often used in Glen's law, is the square root of the second invariant of the strain rate tensor (Cuffey & Paterson, 2010), defined as

$$\dot{\epsilon}_E=\sqrt{\dot{\epsilon}_{xx}^2+\dot{\epsilon}_{yy}^2+\dot{\epsilon}_{xy}^2+\dot{\epsilon}_{xx}\dot{\epsilon}_{yy}}, \tag{5}$$

where incompressibility and $\dot{\epsilon}_{xz}=\dot{\epsilon}_{yz}=0$ (due to negligible tangential tractions at the upper and lower surfaces of the ice shelf) are assumed.

To calculate the strain rate, we first rotate the horizontal velocity vector to the south and east coordinates. Then, we smooth the data with the second-order Savitzky–Golay filter (Savitzky & Golay, 1964) with a square window size of about 4 km (Movie S2). The window size is approximately $10-20$ times the local ice thickness to remove small-scale dynamical effects that are generally not resolvable with commonly used ice flow equations (Bindschadler et al., 1996). Finally, we calculate the dilation strain rate $\dot{\epsilon}_{dilate}$, maximum shear strain rate $\dot{\epsilon}_{shear}$, strain rate along the flow direction $\dot{\epsilon}_{xx}$, and effective strain rate $\dot{\epsilon}_E$ (Movie S4 and S5).

References

Bindschadler, R., Vornberger, P., Blankenship, D., Scambos, T., & Jacobel, R. (1996). Surface velocity and mass balance of ice streams d and e, west antarctica. *Journal of Glaciology*, *42*(142), 461–475.

Cuffey, K. M., & Paterson, W. S. B. (2010). *The physics of glaciers*. Academic Press.

Fattahi, H., Agram, P., & Simons, M. (2016). A network-based enhanced spectral diversity approach for tops time-series analysis. *IEEE Transactions on Geoscience and Remote Sensing*, *55*(2), 777–786.

Giles, A. B., Massom, R. A., & Lytle, V. I. (2008). Fast-ice distribution in east antarctica during 1997 and 1999 determined using radarsat data. *Journal of Geophysical Research: Oceans*, *113*(C2).

Harper, J. T., Humphrey, N., & Pfeffer, W. T. (1998). Crevasse patterns and the strain-rate tensor: a high-resolution comparison. *Journal of Glaciology*, *44*(146), 68–76.

Hetland, E., Musé, P., Simons, M., Lin, Y., Agram, P., & DiCaprio, C. (2012). Multiscale insar time series (mints) analysis of surface deformation. *Journal of Geophysical Research: Solid Earth*, *117*(B2).

Howat, I. M., Porter, C., Smith, B. E., Noh, M.-J., & Morin, P. (2019). The reference elevation model of antarctica. *The Cryosphere*, *13*(2), 665–674.

Mahoney, A., Eicken, H., Graves, A., Shapiro, L., & Cotter, P. (2004). Landfast sea ice extent and variability in the alaskan arctic derived from sar imagery. In *Igarss 2004. 2004 ieee international geoscience and remote sensing symposium* (Vol. 3, pp. 2146–2149).

Mahoney, A., Eicken, H., Shapiro, L., & Graves, A. (2006). Defining and locating the seaward landfast ice edge in northern alaska. In *18th international conference on port and ocean engineering under arctic conditions (poac'05), potsdam, ny* (pp. 991–1001).

Mouginot, J., Scheuchl, B., & Rignot, E. (2017). Measures antarctic boundaries for ipy 2007–2009 from satellite radar, version 2. *National Snow and Ice Data Center*, *10*.

Nye, J. F. (1959). A method of determining the strain-rate tensor at the surface of a glacier. *Journal of Glaciology*, *3*(25), 409–419.

Padman, L., Erofeeva, S. Y., & Fricker, H. A. (2008). Improving antarctic tide models by assimilation of icesat laser altimetry over ice shelves. *Geophysical Research Letters*, *35*(22).

Padman, L., Fricker, H. A., Coleman, R., Howard, S., & Erofeeva, L. (2002). A new tide model for the antarctic ice shelves and seas. *Annals of Glaciology*, *34*, 247–254.

Riel, B., Minchew, B., & Joughin, I. (2021). Observing traveling waves in glaciers with remote sensing: new flexible time series methods and application to sermeq kujalleq (jakobshavn isbræ), greenland. *The Cryosphere*, *15*(1), 407–429.

Riel, B., Simons, M., Agram, P., & Zhan, Z. (2014). Detecting transient signals in geodetic time series using sparse estimation techniques. *Journal of Geophysical Research: Solid Earth*, *119*(6), 5140–5160.

Rosen, P. A., Gurrola, E., Sacco, G. F., & Zebker, H. (2012). The insar scientific computing environment. In *Eusar 2012; 9th european conference on synthetic aperture radar* (pp. 730–733).

Savitzky, A., & Golay, M. J. (1964). Smoothing and differentiation of data by simplified least squares procedures. *Analytical chemistry*, *36*(8), 1627–1639.

Strozzi, T., Luckman, A., Murray, T., Wegmuller, U., & Werner, C. L. (2002). Glacier motion estimation using sar offset-tracking procedures. *IEEE Transactions on Geoscience and Remote Sensing*, *40*(11), 2384–2391.

Strozzi, T., Wegmuller, U., & Matzler, C. (1999). Mapping wet snowcovers with sar interferometry. *International Journal of Remote Sensing*, *20*(12), 2395–2403.

Movie S1.

Time-lapse SAR movie in Larsen B area from Sentinel-1.

Movie S2.

Horizontal velocity in east and south direction after Savitzky–Golay filtered and corresponding SAR image.

Movie S3.

Horizontal velocity maps after time-series filtering.

Movie S4.

Maps of dilation strain rate $\dot{\epsilon}_{dilate}$ and maximum shear strain rate $\dot{\epsilon}_{shear}$.

Movie S5.

Maps of strain rate along the flow direction $\dot{\epsilon}_{xx}$ and effective strain rate $\dot{\epsilon}_{E}$.

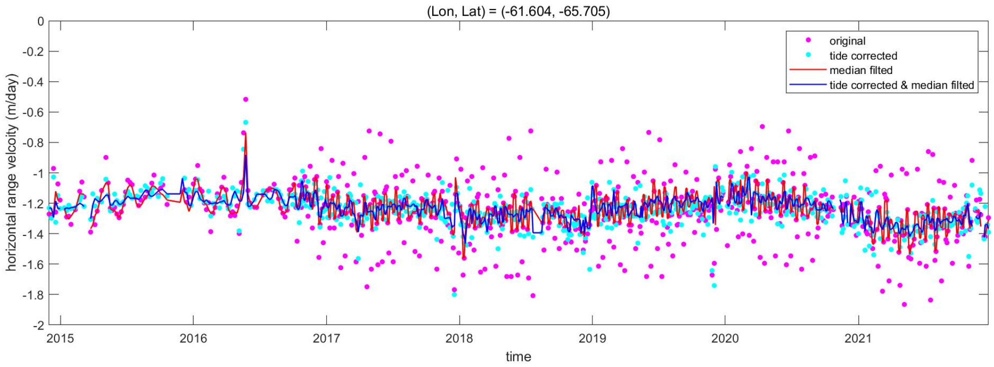

Figure S1. Comparison of horizontal range velocity v_{rh} at one spot on the Scar Inlet Ice Shelf before (red dots) and after tide correction (blue dots). Red and blue lines represent the original and tidal corrected v_{rh} after median filtering.

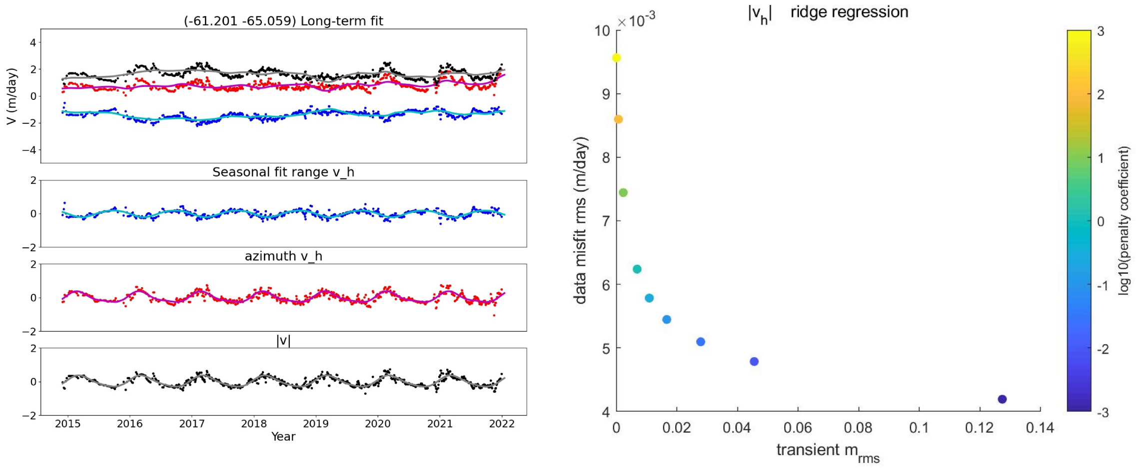

Figure S2. Long-term and seasonal components (a) for a spot on the landfast sea ice and “L curves” for L2-norm regression (b). Solid lines in the upper figures in (a) represent the long-term fitting curves. The seasonal fitting curves (solid lines) and detrended data (dots) are compared in the three lower figures (a). Data misfit and norm of parameter vector are plotted for different penalty coefficients in (b), and the “optimum” coefficient is at the corner of the curve.